Decomposition of strongly charged topological defects

Samo Kralj

Department of Physics,

Faculty of Natural Sciences and Mathematics,

University of Maribor, Koroška cesta 160,

SI-2000 Maribor, Slovenia,

and

Jožef Stefan Institute, P.O. Box 3000,

SI-1000 Ljubljana, Slovenia

Bryce S. Murray and Charles Rosenblatt

Department of Physics, Case Western Reserve University, Cleveland, Ohio 44106-7079, USA

(Dated: February 2, 2017)

Abstract

We study decomposition of geometrically enforced nematic topological defects bearing relatively large defect strengths m in effectively two-dimensional planar systems. Theoretically, defect cores are analyzed within the mesoscopic Landau - De Gennes approach in terms of the tensor nematic order parameter. We demonstrate a robust tendency of defect decomposition into *elementary units* where two qualitatively different scenarios imposing total defect strengths to a nematic region are employed. Some theoretical predictions are verified experimentally, where arrays of defects bearing charges $m = \pm 1$, and even $m = \pm 2$, are enforced within a plane-parallel nematic cell using an AFM scribing method.

PACS numbers: 61.30.Jf, 61.30.Cz

I. INTRODUCTION

Topological defects (TDs) are an unavoidable consequence of continuous symmetry breaking phase transitions and are therefore ubiquitous in nature [1]. They appear at all scales of physical systems, including particle physics, condensed matter and cosmology [2]. Due to their topological origin they display several universalities that are independent of the systems' microscopic details. Understanding their fundamental behavior is therefore of broad interest for all branches of physics. For example, they might even explain stability of "fundamental particles" via the topological protection if *fields* represent a fundamental entity of nature [3, 4]. It is of high interest to find media in which diverse TDs could be created relatively easily, manipulated and observed to resolve several still open fundamental problems.

For this purpose, liquid crystal (LC) phases [5–7] represent an ideal experimental testing ground owing to their extraordinary and unique combination of optical anisotropy, fluidity and softness. Furthermore, they possess a rich variety of different phases and configurations that contain practically all qualitatively different TDs from a symmetry perspective. Consequently, LCs could be exploited as a convenient window into the fundamental behavior of TDs. In addition, TDs in LCs could be employed in diverse applications. For example, it has been demonstrated that TDs in LC phases are efficient traps [8–10] for appropriate (surface decorated) nanoparticles, which opens several opportunities for applications in the realms of functional nano-devices [11], self-assembling processes [12], and for the development of sensitive nanoparticle detectors [13, 14].

The orientationally ordered uniaxial nematic (N) phase is the simplest LC phase [7]. In thermotropic LCs it is reached via the first order phase transition from the isotropic (ordinary liquid) phase, corresponding to the $SO(3) -> O(2)$ symmetry group change. Its local ordering is at the mesoscopic scale presented by the nematic director field $\overrightarrow{n}$, where orientations $\pm\overrightarrow{n}$ are equivalent. In bulk equilibrium $\overrightarrow{n}$ is homogeneously aligned along a symmetry breaking direction. The corresponding order parameter equilibrium manifold is the projective two-sphere S_2/Z_2 of unit radius, where the antipodal points are equivalent.

The nematic phase could exhibit *point* or *line* defects, the centers of which are singular in $\overrightarrow{n}$, and also nonsingular *textures*. The key property of TDs is their topological charge q [7, 15] which is a conserved quantity. In three dimensions (3D) q reveals how many times all possible orientations of $\overrightarrow{n}$ are realized while moving across a closed surface enclosing the defect. In 2D, to

which we effectively restrict our study, the topological charge is equivalent to the winding number m, also referred to as the "Frank index" or "defect strength" [7, 15]. It is defined by $m = \gamma/(2\pi)$ where γ is the rotation angle of $\overrightarrow{n}$ when one circumnavigates the defect line counter-clockwise. Owing to the $\pm\overrightarrow{n}$ symmetry of the nematic phase, m can take on values of $\pm\,1/2, \pm 1, \pm 3/2, \pm 2...$ The defects bearing opposite value of m are commonly referred to as the *defects* ($m > 0$) and *antidefects* ($m < 0$). Pairs $\{m, -m\}$ could annihilate each other into a defect-free state, but isolated TDs with $m \neq 0$ could not be removed. However, in a closed system their number can be changed via annihilation, merging or decomposition of TDs where topological charge conservation rule must be obeyed. Note that a 3D defect, whose local structure is characterized by integer m, could in principle avoid singularity in $\overrightarrow{n}$ by "escaping into the third dimension" [16].

For various potential applications, particular in nanotechnology, it is of interest to stabilize diverse regular patterns of nematic TDs. Namely, templates of TDs could be exploited to create controlled complex arrangements of nanoparticles [10], nanowires [17], or nanosheets [18]. In pioneering studies [19–21] workers have so far succeeded in stabilizing effectively 2D networks of $m = \pm 1$ TDs in nonchiral LCs. Networks consisting of TDs bearing stronger charges have not until now been studied. Furthermore, due to the finite resolution of these studies it is not clear if the cores of TDs bearing $|m| > 1/2$ decompose into smaller units, which is expected due to energetic reasons [7] and allowed by topological charge conservation law.

In this paper we study the decomposition of nematic topological defects in effectively 2D LC patterns. Using a mesoscopic approach we analyze theoretically equilibrium nematic structures in regions to which we impose geometrically different total defect strengths. We also examine the effect of perturbations at the defect core from that of an ideally patterned defect. Finally, we present experimental results in which we pattern defect arrays with an Atomic Force Microscope (AFM) stylus in very thin cells to verify key theoretical predictions.

The plan of the paper is as follows. In Sec. II we describe the mesoscopic Landau-de Gennes model that we use. Numerical outcomes of the modelling are presented in Sec. III. In Sec. IV the experimental set-up, designed to verify theoretical predictions, is described. Key experimental results are assembled and discussed in Sec. V. In the last section we summarize the results and present our future plans.

II. THEORETICAL BACKGROUND

Patterns of nematic topological defects within a flat two-dimensional film, defined by Cartesian coordinates (x, y), can be in general well described by

$$\varphi\left(x,y\right)=\sum_{i=1,N}^{\sim}\left]m_i\tan^{-1}\right)\frac{y-y_i}{x-x_i}\Bigg[+c_i \tag{1}$$

Here N is the number of TDs, and the i-th defect located at the point (x_i, y_i) is characterized by the defect strength m_i and constant c_i. This expression solves the Euler-Lagrange equation [7] if one describes nematic ordering solely in terms of the uniaxial nematic director field $\overrightarrow{n}$ parametrized by the angle φ, assuming equal Frank elastic constants.

For a single isolated defect the local elastic free energy penalty outside the core scales as [7] $\Delta F \propto m_i^2$. Consequently, it is in general energetically advantageous that the defects decompose into *elementary units* bearing charges $m_0 = \pm 1/2$. For example, in the case of a single $m = 1$ defect it holds $\Delta F \propto m^2 = 1$, while if it decomposes into two $m_0 = 1/2$ *elementary units* it follows that $\Delta F \propto \frac{1}{4} + \frac{1}{4} = \frac{1}{2}$.

The focus of our study is to analyze decomposition of topological defects into *elementary* topological defects, both theoretically and experimentally. We set that the LC is confined within a plane-parallel cell where the cell plates are placed at $z = 0$ and $z = h$. In the experimental part of the work we scribe, using an AFM stylus [21], a defect pattern obeying Eq.(1) at the bottom plate. At the top plate the azimuthally degenerate planar alignment is enforced. We consider cases where i) nematic structures within the cell are predominantly influenced by the bottom "master" plate, and ii) the cell thickness h is small enough so that spatial variations in nematic ordering along the z-coordinate could be neglected. Therefore, systems of interest are assumed to be well modelled in two-dimensions. Consequently, we limit the theoretical modelling to nematic structures exhibiting only (x, y) spatial variations. In the theoretical part we use a minimal model to match experimental and theoretical results, where we allow the LC also to locally exhibit biaxial states.

A. Mesoscopic model

We describe the nematic ordering by a tensor nematic order parameter $\underline{Q}$ represented in its eigenframe as [7]

$$\underline{Q} = \sum_{i=1}^{3} \lambda_i \overrightarrow{e}_i \otimes \overrightarrow{e}_i \,, \tag{2}$$

where λ_i are the eigenvalues and $\overrightarrow{e}_i$ the eigenvectors.

For the case of uniaxial nematic ordering, $\underline{Q}$ can be expressed as

$$\underline{Q}^{(u)} = S \Big) \overrightarrow{n} \otimes \overrightarrow{n} - \frac{1}{3}\underline{I} \Big[\,, \tag{3}$$

where S is the uniaxial scalar order parameter, $\overrightarrow{n}$ is the nematic director field, $\otimes$ marks the tensorial product, and $\underline{I}$ stands for the identity tensor. The unit vector $\overrightarrow{n}$ points along the local uniaxial ordering direction and the scalar order parameter S expresses the magnitude of fluctuations about $\overrightarrow{n}$.

Importantly, if elastic distortions are present nematic ordering could exhibit some degree of biaxial ordering. The degree of biaxiality is measured by the scalar parameter [22]

$$\beta^2 = 1 - \frac{6(\mathrm{tr}\underline{Q}^3)^2}{(\mathrm{tr}\underline{Q}^2)^3}, \tag{4}$$

where tr stands for the trace operator and β^2 ranges in the interval $[0, 1]$. Uniaxial configurations correspond to $\beta^2 = 0$. On the other hand, the maximum degree of biaxiality corresponds to $\beta^2 = 1$. The equality $\mathrm{tr}\underline{Q}^3 = 3\mathrm{Det}Q = 3\lambda_1\lambda_2\lambda_3$ reveals that, in the latter case, Q has at least one vanishing eigenvalue.

We express the free energy density of the nematic LC as $f = f_c + f_e$, where the condensation (f_c) and elastic (f_e) contribution are expressed as [7, 23]

$$f_c = A_0(T - T_*)\mathrm{tr}\underline{Q}^2 - B\mathrm{tr}\underline{Q}^3 + C(\mathrm{tr}\underline{Q}^2)^2, \tag{5}$$

$$f_e = \frac{L}{2}|\nabla \underline{Q}|^2 \,. \tag{6}$$

Here A_0, B, and C are material constants, T_* is the supercooling temperature of the isotropic phase, T stands for the temperature, and L is the nematic elastic constant in the one-constant approximation. In bulk the condensation term enforces the Isotropic-Nematic (*I-N*) phase transition at the critical temperature $T_{IN} = T_* + B^2/(24A_0C)$.

We mimic a confining surface with imposed local orientational ordering by the field-like term [24]

$$f_f = \frac{w}{2}\mathrm{tr}\Big)\underline{Q} - \underline{Q}_s\Big(^2. \tag{7}$$

The strength of surface imposed anchoring is measured by a positive anchoring constant w and $\underline{Q}_s$ describes the nematic ordering imposed by the confining substrate. In the strong anchoring limit $w \to \infty$, it holds that $\underline{Q} = \underline{Q}_s$. For example, if a uniaxial orientational ordering is enforced along a unit vector $\overrightarrow{e}_s$, then

$$\underline{Q}_s^{(u)} = S_s \Big)\overrightarrow{e}_s \otimes \overrightarrow{e}_s - \frac{1}{3}\underline{I}\Big[\ , \tag{8}$$

where S_s describes the surface enforced degree of uniaxial ordering.

B. Parametrization

We parametrize the $\underline{Q}$-tensor order parameter as [25, 26]

$$\underline{Q} = (q_3+q_1)\overrightarrow{e}_x \otimes \overrightarrow{e}_x + (q_3-q_1)\overrightarrow{e}_y \otimes \overrightarrow{e}_y + q_2(\overrightarrow{e}_x \otimes \overrightarrow{e}_y + \overrightarrow{e}_y \otimes \overrightarrow{e}_x) - 2q_3\overrightarrow{e}_z \otimes \overrightarrow{e}_z, \tag{9}$$

where $q_1(x,y)$, $q_2(x,y)$, and $q_3(x,y)$ are variational order parameters. In this parametrization we set that $\overrightarrow{e}_3 = \overrightarrow{e}_z$ is always an eigenvector of $\underline{Q}$. The remaining two eigenvectors $\{\overrightarrow{e}_1, \overrightarrow{e}_2\}$ are allowed to rotate within the $(\overrightarrow{e}_x, \overrightarrow{e}_y)$ plane:

$$\begin{aligned} \overrightarrow{e}_1 &= \cos\varphi\,\overrightarrow{e}_x + \sin\varphi\,\overrightarrow{e}_y, \\ \overrightarrow{e}_2 &= -\sin\varphi\,\overrightarrow{e}_x + \cos\varphi\,\overrightarrow{e}_y, \\ \overrightarrow{e}_3 &= \overrightarrow{e}_z. \end{aligned} \tag{10}$$

In terms of $\{q_1,\ q_2,\ q_3\}$ the three $\underline{Q}$ eigenvalues are expressed as $s_1 = q_3 + \sqrt{q_1^2+q_2^2}$, $s_2 = q_3 - \sqrt{q_1^2+q_2^2}$ and $s_3 = -2q_3$. The exchange [27] of eigenvalues $s_1 \leftrightarrow s_2$ is realized when $\sqrt{q_1^2+q_2^2} = 0$. In the case of uniaxial ordering (see Eq.(3)), where we enforce $\overrightarrow{n} = \overrightarrow{e}_1$, it holds that

$$q_1 = S\cos(2\varphi)/2, q_2 = S\sin(2\varphi)/2, q_3 = S/6. \tag{11}$$

To visualize the topology of possible nematic structures we employ the following alternative parametrization of the $\underline{Q}$ eigenvalues [25]

$$\begin{aligned} \lambda_1 &= \frac{2}{3} s \cos\psi, \\ \lambda_2 &= -\frac{2}{3} s \cos\Big)\psi - \frac{\pi}{3}\Big(, \\ \lambda_3 &= -\frac{2}{3} s \cos\Big)\psi + \frac{\pi}{3}\Big(, \end{aligned} \tag{12}$$

where

$$s = \sqrt{\frac{3}{2} \mathrm{tr} \underline{Q}^2}. \tag{13}$$

The case $s = 0$ corresponds to an isotropic state. Furthermore, the biaxiality measure can be expressed as $\beta^2 = \sin^2(3\psi)$. Possible nematic configurations on varying ψ for a finite value of s for a fixed $\underline{Q}$-eigenframe are shown in **Fig. 1**. Configurations $\{\psi = 0, \psi = 2\pi/3, \psi = -2\pi/3\}$ correspond to uniaxial states with a positive scalar order parameter S (see Eq.(3)), and $\{\psi = \pi, \psi = -\pi/3, \psi = \pi/3\}$ to uniaxial states with a negative value of S for the the nematic director aligned along $\overrightarrow{e}_1$, $\overrightarrow{e}_2$, and $\overrightarrow{e}_3$, respectively. The degree of maximal biaxiality is realized for $\psi = \pm\pi/6$, $\psi = \pm\pi/2$, and $\psi = \pm 5\pi/6$.

C. Scaling and dimensionless equilibrium equations

In order to rewrite the free energy in a dimensionless form we introduce dimensionless and scaled quantities. We introduce the reduced temperature [26]

$$\theta = \frac{64AC}{3B^2} = \frac{T - T_*}{T_{**} - T_*}, \tag{14}$$

where T_{**} is the nematic superheating temperature. The corresponding superheating bulk nematic order parameter S_{**} is given by

$$S_{**} = \frac{3B}{16C}. \tag{15}$$

In terms of these quantities the equilibrium scalar order parameter corresponding to a global minimum in a bulk homogeneous uniaxial configuration exists for $\theta \leq \frac{T_{IN} - T_*}{T_{**} - T_*} = \frac{8}{9}$ and can be expressed as

$$S_{eq} = S_{**}\Big)1 + \sqrt{1 - \theta}\Big(. \tag{16}$$

Competing metastable states exist within the reduced temperature window $\theta \in [0, 1]$. It is convenient to scale the nematic order parameter with respect to S_{**}, therefore we introduce $\underset{\vee}{Q} = \underline{Q}/S_{**}$, $\underset{\vee}{Q}_s = \underline{Q}_s/S_{**}$; *i.e.*, $\underset{\vee}{q}_1 = q_1/S_{**}$, $\underset{\vee}{q}_2 = q_2/S_{**}$, $\underset{\vee}{q}_3 = q_3/S_{**}$, $\underset{\vee}{S}_s = S_s/S_{**}$.

An important role in our modelling is played by the biaxial order parameter correlation length ξ_b, which roughly estimates the linear core size of common topological defects. Its size is estimated by [26]

$$\xi_b = \frac{4}{3} \quad \frac{LC}{B^2 \ \sqrt{1-\theta}+1} = \frac{\xi_b^{(0)}}{\sqrt{\tau}}. \tag{17}$$

where $\xi_b^{(0)} = \frac{4\sqrt{LC}}{3B}$ is the bare biaxial correlation length and $\tau = \sqrt{1-\theta}+1$. For example, for the liquid crystal pentylcyanobiphenyl (5CB) it holds [28] that $\xi_b \sim 30 \pm 10$ nm. We further scale all lengths in units of h and introduce the dimensionless operator $\nabla = h\nabla$. It follows that

$$f_c = A_e^2 \Big) \frac{\theta}{6}(q_1^2+q_2^2+3q_3^2) - 2q_3(q_1^2+q_2^2-q_3^2) + \frac{1}{4}(q_1^2+q_2^2+3q_3^2)^2 \Big[, \tag{18}$$

$$f_e = |\nabla q_1|^2 + |\nabla q_2|^2 + 3\,|\nabla q_3|^2 , \tag{19}$$

$$f_s = A_s \mathrm{tr} \Big) \underline{Q} - \underline{Q}_s \Big(^2 . \tag{20}$$

In the equations above we omitted the tildes, $\{f_c, f_e, f_s\}$ are dimensionless free energy densities, and $A_e = h/\xi_b^{(0)}$ and $A_s = h^2 w/L$ are dimensionless quantities. In the expression for the surface interaction we enforce uniaxial ordering, see Eq.(8). We set

$$\overrightarrow{e}_s = \cos\varphi_s \, \overrightarrow{e}_x + \sin\varphi_s \, \overrightarrow{e}_y, \tag{21}$$

$$\frac{1}{2}\mathrm{tr} \Big) \underline{Q} - \underline{Q}_s \Big(^2 = q_1^2 + q_2^2 + 3q_3^2 - q_3 S_s + \frac{S_s^2}{3} - S_s \left(q_1 \cos(2\varphi_s) + q_2 \sin(2\varphi_s)\right). \tag{22}$$

III. NUMERICAL OUTCOMES

Of interest are configurations of topological defects that are stabilized in plane-parallel ("planar") geometries exhibiting effectively two-dimensional (x, y) behavior. We study two different surface imposed anchoring conditions, to which we henceforth refer as the *boundary anchoring condition* (BAC) and *field anchoring condition* (FAC), respectively.

In BAC we strongly impose the uniaxial nematic structure (i.e. $A_s \to \infty$, see Eq.(8), Eq.(21), Eq.(22)) defined as

$$\varphi_s(x, y) = m \tan^{-1} \Big) \frac{y}{x} \Big(\tag{23}$$

on a circle of radius $R = \sqrt{x^2+y^2} >> \xi_b$. Within the region $R < \sqrt{x^2+y^2}$ we impose degenerate tangential anchoring. The ansatz Eq.(23) defines TDs exhibiting uniaxial structure characterized by the winding number $m \in [\pm 1/2, \pm 1, \pm 3/2, \pm 2....]$, with the defect's center located at $(x = 0, y = 0)$. The conservation law of topological charges dictates that nematic structures within the region $R < \sqrt{x^2+y^2}$ must exhibit the imposed total charge m.

In FAC we impose the surface field-type anchoring defined by Eq.(20), where φ_s is determined by Eq.(23) and $S_s = S_{eq}$ (see Eq.(16)).

Note that TDs bearing $m_0 = \pm 1/2$ are from the $\beta^2(x, y)$ perspective characterized by a $\beta^2 = 1$ rim. The rim separates the interior region exhibiting essentially negative uniaxiality from the outer region where nematic ordering displays essentially positive uniaxiality, as demonstrated in **Figs. 2** where we plot the $\beta^2(x, y)$ dependence of a single $m_0 = 1/2$ defects. In bulk and in the approximation of a single nematic elastic constant, an isolated $m_0 = \pm 1/2$ defect possesses a circularly shaped rim. For example, when crossing the core of $m_0 = 1/2$ defect (see the line in **Fig. 2a**) one moves in order parameter space $\{s, \psi\}$ from, e.g., uniaxial ordering along $\overrightarrow{n} = \overrightarrow{e}_1$ towards $\overrightarrow{n} = \overrightarrow{e}_2$, as indicated by the dashed red line in **Fig. 1**.

In the following we study TDs enforced by BAC and FAC. The structures were calculated numerically by solving the corresponding Euler-Lagrange equations resulting from the free energy minimization. Note that the core structures of $\pm m$ defects have identical $\beta^2(x, y)$ structure in the single nematic elastic constant approximation. For this reason we consider only cases with $m > 0$.

A. Boundary anchoring condition

We first study TDs using BAC. In **Figs. 3** we plot TDs for cases where we enforce $m = 1$ (**Fig. 3a**), $m = 2$ (**Fig. 3b**), $m = 3$ (**Fig. 3c**), and $m = 4$ (**Fig. 3d**). One sees that in all cases there exist only TDs exhibiting unit charges $m_0 = 1/2$. The TDs repel each other and consequently they tend to assemble close to the bounding circle at which we enforce a total topological charge m for the LC configurations.

B. Field anchoring condition

We further consider cases where we enforce TDs via FAC by gradually increasing the dimensionless field anchoring strength A_s (Eq.(20)). In **Figs. 4** (**Figs. 5**) we show cases where we

enforce a single defect bearing $m = 1$ ($m = 2$) on increasing A_s. For both values of m we see that for a relatively weak anchoring strength A_s the single defects are always decomposed into TDs bearing *elementary* charges. On increasing A_s the TDs are progressively dragged together and at a critical value of $A_s = A_s^{(c)}(m)$ the TDs merge into a single TD bearing the topological charge m. At the critical condition the separate $\beta^2 = 1$ rims of TDs bearing $m = m_0$ (existing for $A_s < A_s^{(c)}(m)$) merge into a single $\beta^2 = 1$ rim. For the parameter set $\{A_e = 10, \tau = 4\}$ we find $A_s^{(c)}(1) \sim 0.45$ and $A_s^{(c)}(2) \sim 1.3$. Note that for $A_s = A_s^{(c)}$ the core structure of the single defect exhibits essentially negative uniaxiality in all cases studied, which is separated from the surrounding nematic structure displaying essentially positive uniaxiality by the rim possessing maximal biaxiality.

Note that these two-dimensional structures (see **Fig. 4c** and **Fig. 5c**) of relatively strongly charged TDs possess cores exhibiting essentially *negative* uniaxiality. A typical trajectory on crossing cores of such TDs is sketched by the dashed red line in **Fig. 1**.

We next analyze the robustness of defects patterns with respect to imperfections. For this purpose we introduce, at different positions, square *perturbation patches* of characteristic length h_p, within which we enforce, in addition to FAC, a local perturbation field described by Eq. (20) of strength $A_s^{(p)}$. In it we enforce uniaxial uniform ordering along a fixed orientation $\varphi_s^{(p)}$, using parametrization Eq.(21). The center of the imposed "total" defect is set at $(x, y) = (0, 0)$ and the center of a *perturbation patch* is placed at (x_p, y_p), where values of displacements $\{x_p, y_p\}$ and h_p are comparable to ξ_b. With these *patches* we approximately mimic imperfections in the patterns using the AFM scribing method; see next section. Some representative examples are presented in **Figs. 6**. One sees that the shape and orientations of daughter defects could in general be strongly influenced by relatively weak local imperfections.

IV. EXPERIMENTAL SET-UP

In our effectively 2D theoretical analysis we impose the defect patterns by *field anchoring condition* term Eq.(7). A possible experimental realization of such conditions is by confining a nematic LC in a thin plane-parallel cell, where one "master" surface imposes anchoring conditions described by Eq.(7) and the other imposes degenerate tangential (planar) anchoring condition. If the cell is thin enough, as demonstrated in Ref.[21], the nematic pattern within the cell is controlled by the master plate, and the resulting pattern is effectively 2D. To mimic this case we set that the

field term given by Eq.(7) is present only at the master plate of the 3D plane-parallel cell. Taking this into account, the dimensionless surface anchoring coefficient A_s in Eq.(20) is expressed as

$$A_s = \frac{h}{d_e}. \tag{24}$$

Here $d_e = L/w_m$ is the surface extrapolation length [7, 23], and $w_m = wh$ is the "conventional" anchoring strength. Note that by using the definition Eq.(7) it holds that $[w] = N/m^2$. In the following we describe in detail the corresponding experimental set-up in which such conditions are realized.

The goal of the experimental work is to create artificially controlled topological defects in a liquid crystal cell that facilitate an examination of some of the theoretical predictions. Details of the experimental cell preparation are described elsewhere [21]. Briefly, a glass substrate was spin coated with polyamic acid RN-1175 (Nissan Chemical Industries) and baked according to the manufacturer's specifications to imidize. The resulting polyimide layer first was rubbed gently with a polyester cloth (Yoshikawa YA-20-R) and then scribed strongly with a pattern, defined by Eq.(1), using the stylus of an atomic force microscope (AFM). (The purpose of the initial weak cloth rubbing was to minimize the director discontinuity at the edges of the AFM lithography; within the AFM scribed region, however, the scribed pattern overwhelmed the gentle background rubbing.) An AFM stylus force of 2.5 μN was used to create two types of easy axis checkerboard patterns of dimensions 90x90 μm, with the depth of the scribed lines being about 15 nm. One pattern had topological defects of strength $m = \pm 1$ arranged in a 3 x 3 square array, with defect cores spaced approximately 30 μm apart (**Fig. 7a**); the other pattern also was a 3 x 3 array, but with topological defects having strength $m = \pm 2$ (**Fig. 8a**). Each line was scribed randomly in one direction or the opposite direction, as chosen by a computer-generated coin toss. Thus on average the local scribing direction was random with a binomial distribution, thereby minimizing residual pretilt of the director at the surface that could have arisen from unidirectional scribing. The separation between the scribe lines varied from approximately 300 nm in regions of low curvature to 100 nm in regions of high curvature, see **Fig. 9**. As the scribing process is analogous to plowing, polyimide debris was present, which was removed by sonication in ethanol. For any regular array of defects, if the sum of the defect strengths were zero, the director field would relax to the background rubbing angle far from the defects. However, none of our defect arrays was topological-charge neutral, and thus we observed some unwanted edge behavior, although it did not affect the area of interest.

To create a closed cell, a second substrate was coated with Glymo [(3-glycidyloxypropyl) trimethoxysilane; Sigma-Aldrich], which serves as an azimuthally degenerate layer for planar alignment. The patterned and the degenerate substrates were placed together with mylar spacers and clamped. The cell thicknesses, as determined by interferometry, varied between 2 and 5 μm. This spacing was less than the defect core spacing of 30 μm, and thus the azimuthal director orientation does not relax significantly on moving away from the scribed surface into the bulk. The cell was filled with the liquid crystal 5CB in the in the isotropic phase and cooled through the isotropic-nematic transition temperature T_{IN} = 35^0C to stabilize room temperature.

V. EXPERIMENTAL MEASUREMENTS AND DISCUSSION

The director pattern of each cell, described in the experimental set up section, was imaged using a polarizing microscope; the images are shown in **Fig. 7b** and **Fig. 8b**. The most obvious cases of defect decomposition can be seen in the extinction pattern caused by the director field. However, the daughter defects are most easily observed as dark spots in unpolarized brightfield transmission microscopy (**Figs. 7c** and **Figs. 8c**) or as bright spots when viewed under unpolarized darkfield. These images provide better detail about the location and size of the defect cores than those obtained by polarized microscopy, and are clearly due to light scattering from the cores in which the refractive indices are varying rapidly in space. If a scribed core has not decomposed into "daughter defects", it is not possible with these microscopy methods to determine whether the core has, in fact, split on a scale that is smaller than the optical resolution of the instrument.

Note that the cores of $m = \pm 1/2$ line defects are always biaxial [27, 29]. A typical biaxial topology in the *perpendicular plane* (a plane perpendicular to the direction of a line defect, i.e. (x, y) plane in our modelling) is plotted in **Fig. 2**. The characteristic linear size of the defect's core is roughly given by the biaxial correlation length [29]. For the case of localized distortions characterized by $m = \pm 1$, there are several options. In sufficiently thin cells singular line defects might be formed. In general, their cores are expected [25] to be essentially biaxial with either i) negative or ii) positive uniaxiality at the center of the core. In these cases the core structure in a *perpendicular plane* is characterized by i) one and ii) two essentially concentric rims exhibiting maximal degree of biaxiality [25]. In both cases the core size region is roughly given by the biaxial order parameter correlation length. Close enough to the *I-N* phase transition and for appropriate elastic properties, the $m = \pm 1$ defect cores could be uniaxial, where the center of the defect

core is isotropic [30–32]. In this case the core size is determined by the uniaxial order parameter correlation length. If the cell thickness is large enough then the nematic director field is expected to "escape along the third direction" [16] to avoid a singularity in $\overrightarrow{n}$. In this case the localized distortion is essentially uniaxial and the characteristic size of *perpendicular plane* distortions is expected to be comparable to the cell thickness. However, our current imaging techniques cannot determine whether the director has adopted an escaped configuration. The escaped configuration can be probed via a Freedericksz-type measurement, however, and is the subject of future work. The cores of defects characterized by $|m| > 1$ have not yet been theoretically analyzed and have been so far only rarely experimentally detected [33].

Even though the spatial resolution of the AFM is very good, there necessarily will be a region at each defect core that is ill-defined. The exact size of this region is difficult to control, but is generally close to 250-500 nm, and not generally larger than one micrometer in diameter. The surface topography for an $m = +2$ defect is shown in **Fig. 9**. The anchoring in the centermost area of this particular defect is effectively random due to overlapping surface manipulations of the AFM stylus. In other cases, the centermost region could be untouched by the tip and therefore provide uniform anchoring due to the prior weak cloth rubbing. In either case, the patterned region scribed by the AFM creates anchoring conditions in the form of a topological defect to within some length scale of the singularity. The undefined central core amounts to, at most, a perturbation of the anchoring. The perturbation near the singularity can cause the daughter defects to differ in size, and can influence the axes along which the defect divides. In the array of singly charged defects shown in **Fig. 7c**, eight of the defects have divided into two half charge defects as predicted by the model. The other scribed defect appears as a single core, which could be due to either limitations in optical resolution or perhaps an escaped configuration. In the $m = \pm 2$ array of **Fig. 8c**, six of the nine initial defects have broken into four half-integer charges located at the corners of a square. The other three have broken into a pair of half-integer cores, with the remainder of the "charge" left in a defect that also appears to be decomposed, but perpendicular in direction and on a smaller length scale. It is likely that this behavior is caused by perturbations in the alignment field that occurred during scribing.

In **Fig. 10a** we calculate the enforced $m = 2$ defect decomposition, where simulation parameters are set to mimic experimental conditions with which the defect textures shown in **Figs. 8** are obtained. Assuming $h \sim 3$ μm, $\xi_b^{(0)} \sim 30$ nm we set $A_e = h/\xi_b^{(0)} = 100$. The separation between adjacent $m_0 = 1/2$ defect is typically 5 μm, which we reproduce in simulations for

$A_s \sim 0.1$. Taking into account Eq.(1), approximating elastic properties by $L \sim 10^{-11}$ N [7], one gets $w_m \sim 10^{-6}$ N/m. Furthermore, **Fig. 10b,c,d** reveal that in the calculated regime the relative placement of "daughter defects" strongly depends on local imperfections. For example, by varying positions of *perturbation patches* (see Sec. III.B) and local preferential ordering within them, one can relatively strongly modify the defect patterns, and the resulting configurations could be strongly asymmetric.

VI. CONCLUSIONS

We studied decomposition of nematic TDs in effectively 2D planar systems, where we enforce a relatively large total topological charge m. The simple Frank modelling, where nematic ordering is described solely with the nematic director field $\overrightarrow{n}$, suggests that for the case of a single defect bearing charge m, its local elastic cost ΔF scales as $\Delta F \sim m^2$. Consequently, the general tendency is that defects with $|m| > |m_0|$ decompose into TDs bearing *elementary* charges m_0. Due to the so called head-to-tail nematic symmetry, it holds that $m_0 = \pm 1/2$. We tested the robustness of this tendency both theoretically and experimentally for NLC confined to simple planar geometries.

In the theoretical part we employed the Landau-de Gennes approach in terms of the nematic tensor order parameter using the single nematic elastic constant approximation. We focused on the structural behavior of TDs in 2D Cartesian system. We enforced relatively large total topological charge m using two qualitatively different scenarios to which we refer as the *boundary anchoring condition* (BAC) and *field anchoring condition* (FAC). Note that results were tested for both $m > 0$ and $m < 0$. However, resulting biaxial profiles were exactly the same for both cases $\pm |m|$. For this reason we considered only cases with $m > 0$. It needs to be mentioned that this symmetry is a consequence of the single nematic elastic approximation. However, (conventional) elastic anisotropy would, in general, give rise only to quantitative changes without affecting the basic qualitative results.

In the BAC case we imposed the total charge m via the prescribed uniaxial nematic director pattern on a circle of a radius $R >> \xi_b$ which encircles nematic LC phase. We treated cases with $m = 1$, 2, 3 and 4 relatively deep into the nematic phase. Simulations revealed that, in equilibrium, the system always consisted only of *elementary* TDs with charges $m_0 = 1/2$. In all cases the topological charge conservation law was obeyed, *i.e.*, $m = N m_0$, where N is the number

of TDs. For relatively large values of m ($m >> 1$), TDs tend to assemble close to the enclosing circle, which becomes increasingly pronounced on increasing the ratio R/ξ_b. This phenomenon is reminiscent of the *Faraday effect* in electrostatics and will be analyzed in more detail in our future study. Note, that nematic LCs under certain conditions display several remarkable analogies [34–37] with electrostatics, because interactions between TDs often exhibit Coulumb-like coupling.

In the FAC case we enforced single uniaxial defects with dimensionless field strength A_s. In cases of simple plane-parallel geometries of thickness h, where such defect structures are enforced via bounding plates, it holds that $A_s \sim h/d_e$. We find that below the critical value of $A_s^{(c)}(m)$ a single defect decomposes into *elementary* defects. We find $A_s^{(c)}(1) \sim 0.45$ and $A_s^{(c)}(2) \sim 1.3$ for $m = 1$ and $m = 2$, respectively. Note that for $A_s = A_s^{(c)}$ the core structure of single defect exhibits essentially negative uniaxiality in all cases studied, which is separated from the surrounding nematic structure displaying essentially positive uniaxiality by the rim possessing maximal biaxiality.

Experimentally, we studied systems which are relatively well described by FAC. Namely, we confined the LC into plane-parallel cells, where we enforced uniaxial-like defects at one confining plate. We scribed regular patterns enforcing locally either alternating $m = \pm 1$ or $m = \pm 2$ planar defect structures. In three dimensions such patterning enforces line defects, which propagate through the whole cell if h is not too large [21]. Also, line defects described by the winding number $|m| = 1/2$ must either originate and terminate at confining surfaces or form closed loops. However, line defects with $|m| = 1$ might be unstable with respect to the "escape into the third dimension". In both samples splitting of TDs into *elementary* TDs were most often observed. This indicates that the effective anchoring strength is below its critical strength, which in simulations is quantified by $A_s^{(c)}$.

We note that that the core size of an $|m| = 1/2$ defect is larger than, but comparable to the biaxial correlation length ξ_b, which for 5CB is estimated to be in the range between 20 and 40 nm. ξ_b is the distance over which locally induced biaxial degree of order relaxes. Such lengths are smaller than visible light resolution. However, the enforced $|m| = 1$ and $|m| = 2$ core structures are larger because of stronger elastic distortions and also more easily visible because they are larger than a biaxial correlation length by a factor ˜4 to 6 (See Fig. 2). Moreover, Furthermore, the daughter line defects might exhibit some spatial variations along the z-axis, as our preliminary 3D simulations reveal. Namely, the scribed surface patterns tend to prevent decomposition of the defects, which contradicts the bulk tendency. The simulations reveal that the resulting structures

exhibit spatial variations along the z-axis, which increases the effective core size of structures measured at supramesoscopic level

In our future study we intend to analyze possible structures of a topologically enforced $m = 1$ defect in a plane-parallel cell on varying the cell thickness and in the presence of an applied electric field. Of particular interest will be the crossover between the non-singular *escaped* $m = 1$ structure [16] and the structure consisting of two "daughter" $m_0 = 1/2$ defects, including biaxiality.

The results of our study are interesting both for potential applications and fundamental physics. Namely, it is of interest to develop methods to stabilize, localize, or even destabilize defects bearing strongly charged TDs. Such defects have unique optical fingerprint which could be exploited in various nano-photonic applications. Furthermore, lattices of strongly charged TDs could be exploited as efficient traps for appropriately surface decorated nanoparticles. The former could form a network bearing specific emergent functionality. By manipulating number or position of TDs one could indirectly influence nanoparticle (super-)structures and, consequently, their functionality. From a fundamental perspective, for example, it is of particular interest to understand under what conditions a certain assembly of *elementary units* remains confined and merges into a single defect bearing a relatively large topological charge.

Acknowledgments

SK was supported by Slovenian Research Agency (ARRS) P1-0099. BSM and CR were supported by the National Science Foundation's Condensed Matter Physics program under grant DMR1505389.

Figure captions

Fig. 1 The phase space (s, ψ) revealing possible nematic states. Solid lines: positively uniaxial states ($S > 0$); $\overrightarrow{n}[\psi = 0] = \overrightarrow{e}_1, \overrightarrow{n}[\psi = 2\pi/3] = \overrightarrow{e}_2, \overrightarrow{n}[\psi = -2\pi/3] = \overrightarrow{e}_3$. Dashed lines: negatively uniaxial states ($S < 0$); $\overrightarrow{n}[\psi = \pi] = \overrightarrow{e}_1, \overrightarrow{n}[\psi = -\pi/3] = \overrightarrow{e}_2, \overrightarrow{n}[\psi = \pi/3] = \overrightarrow{e}_3$. Dotted lines: states with maximal degree of biaxiality $\beta^2 = 1$. The parameter s attains its maximum value on the circle, and the center of the circle corresponds to the isotropic phase, $s = 0$. The dashed red line indicates a trajectory in the order parameter space $\{s, \psi\}$ joining the points A and B (uniaxial states) of the $m = 1/2$ defect core structure depicted in **Fig. 2**.

Fig. 2 A characteristic degree of biaxiality $\beta^2(x, y)$ plot of a $m_0 = 1/2$ topological defect: a) top view with the color code of $\beta^2 \in [0, 1]$, b) side view. The dashed line indicates a path joining states $\overrightarrow{n} = \overrightarrow{e}_1$ with positive uniaxiality (point B) and $\overrightarrow{n} = \overrightarrow{e}_2$ with negative uniaxiality (point A). The corresponding path in the order parameter space $\{s, \psi\}$ is depicted in **Fig. 1** with a dashed

red line.

Fig. 3 $\beta^2(x,y)$ plots of configurations of TDs where we impose via BAC: a) $m=1$, b) $m=2$, c) $m=3$, d) and $m=4$. In all cases only TDs exhibiting unit charge $m_0=1/2$ exist. $A_e=8$, $\tau=4$.

Fig. 4 $\beta^2(x,y)$ plots of configurations of TDs where we impose via FAC single $m=1$ defect. a) $A_s=0.3$, b) $A_s=0.44$, c) $A_s=0.45$. $A_e=10$, $\tau=4$. In **Fig. 4c** we indicate a trajectory that transverses the core of TD. Here B indicates a point where nematic ordering exhibits essentially positive uniaxiality, and A marks a point where the order displays negative uniaxiality. The corresponding trajectory in the order parameter space $\{s,\psi\}$ is schematically sketched in **Fig. 1** by a dashed red line.

Fig. 5 $\beta^2(x,y)$ plots of configurations of TDs where we impose via FAC single $m=2$ defect. a) $A_s=0.8$, b) $A_s=1.2$, c) $A_s=1.3$. $A_e=10$, $\tau=4$. In **Fig. 5c** we indicate a trajectory which transverses the core of TD. Here B indicates a point where nematic ordering exhibits essentially positive uniaxiality, and A marks a point where the order displays negative uniaxiality. The corresponding trajectory in the order parameter space $\{s,\psi\}$ is schematically sketched in **Fig. 1** by a dashed red line.

Fig. 6 $\beta^2(x,y)$ plots of configurations of TDs where we impose via FAC a $m=2$ defect centered at $(x=0,y=0)$. The defect is decomposed into four $m=1/2$ daughter TDs. The spatial orientation of their cores is affected by different local perturbations. a) $A_s^{(p)}=0$; b) $A_s^{(p)}=1$, $\varphi_s^{(p)}=0$; c) $A_s^{(p)}=1$, $\varphi_s^{(p)}=\pi/2$; d) $A_s^{(p)}=0.1$, $\varphi_s^{(p)}=\pi/2$. In all figures we set $A_e=30$, $A_s=1$, $\tau=4$. The center of the perturbation patch of size $h_p=\xi_b/2$ was imposed at coordinates $(x_p=\xi_b/2, y_p=\xi_b/2)$.

Fig. 7 a) Schematic representation of the "easy axis" director pattern of a 3x3 array of $m=\pm1$ topological defects. Filled circles correspond to positive defects and open circles to negative defects. **b)** Extinction resulting from the scribed director pattern. Image taken by polarized microscopy. The polarizer and analyzer are crossed and oriented parallel/perpendicular to the horizontal. **c)** A brightfield microscopy image of the defect cores from **(b)**. Each core is visible as a dark spot due to light scattering. The rows of three spots at the top and bottom of the image, partially obscured by the yellow square, are due to director discontinuities at the boundaries between the scribed square and outer region. The yellow boxes nominally denote the boundaries of the AFM lithography on each image. Scale: 30 μm rectilinear distance between scribed defect cores.

Fig. 8 Same as **Fig. 7** except for $m=\pm2$ topological defects.

Fig. 9 Scribed surface topography as scanned by an Agilent 5500 AFM and a TAP300 non-contact stylus. Non-contact mode was used to avoid damaging the topography. Scale bar = 250 nm.

Fig. 10 $\beta^2(x,y)$ plots of configurations of TDs calculated using FAC. The defect of the strength $m = 2$ is enforced at the center of the figure, where $(x = 0, y = 0)$. We chose typical length scales which were roughly used in the experimental set-up shown in **Fig. 8**, consequently $A_e = h/\xi_b^{(0)} = 100$. The center of the perturbation patch of size $h_p = \xi_b$ was imposed at coordinates (x_p, y_p). a) The reference pattern with $A_s^{(p)} = 0$; b) $(x_p = h/10, y_p = h/10)$, $\varphi_s^{(p)} = \pi/4$, $A_s^{(p)} = 0.1$; c) $(x_p = h/5, y_p = h/5)$, $\varphi_s^{(p)} = 0$, $A_s^{(p)} = 0.1$; d) $(x_p = h/5, y_p = h/5)$, $\varphi_s^{(p)} = \pi/4$, $A_s^{(p)} = 0.1$. In all cases $A_s = 0.1$, $\tau = 4$.

---

[1] N. Mermin, Rev. Mod. Phys. **51**, 591 (1979).

[2] W. H. Zurek, Nature **317**, 505 (1985).

[3] T. Skyrme, Nucl. Phys. **31**, 556 (1962).

[4] A. Hobson, Amer. J. Phys. **81**, 211 (2013).

[5] P. Collings and J. Patel, *Handbook of Liquid Crystal Physics* (Oxford University Press, Oxford, 1997).

[6] M. Kleman and O. Lavrentovich, Phil. Mag. **25-26**, 4117 (2006).

[7] M. Kleman and O. D. Lavrentovich, *Soft Matter Physics* (Springer, New York, 2003).

[8] H. Kikuchi, M. Yokota, Y. Hisakado, H. Yang, and T. Kajiyama, Nat. Mater. **1**, 64 (2002).

[9] B. Roi, V. Tzitzios, E. Karatairi, U. Tkalec, G. Nounesis, Z. Kutnjak, G. Cordoyiannis, R. Rosso, E. Virga, I. Muevi, et al., Eur. Phys. J. E **34**, 17 (2011).

[10] D. Coursault, J. Grand, B. Zappone, H. Ayeb, G. Levi, N. Félidj, and E. Lacaze, Adv. Mater. **24**, 1461 (2012).

[11] Q. Liu, Y. Cui, D. Gardner, X. Li, S. He, and I. Smalyukh, Nano Lett. **10**, 1347 (2010).

[12] D. Nelson, Nano Lett. **2**, 1125 (2002).

[13] M. Brake, M. Daschner, Y. Luk, and N. Abbott, Science **302**, 2094 (2003).

[14] V. Dubtsov, S. V. Pasechnik, D. V. Shmeliova, and S. Kralj, Appl. Phys. Lett. **105**, 151606 (2014).

[15] O. Lavrentovich, Liq.Cryst. **24**, 117 (1998).

[16] P. E. Cladis and M. Kleman, J. Phys. (Paris) **33**, 591 (1972).

[17] J.-B. Fleury, D. Pires, and Y. Galerne, Phys. Rev. Lett. **103**, 267801 (2009).

[18] M. Lavri, V. Tzitzios, S. Kralj, G. Cordoyiannis, I. Lelidis, G. Nounesis, V. Georgakilas, H. Amenitsch, A. Zidansek, and Z. Kutnjak, Appl. Phys. Lett. **103**, 143116 (2013).

[19] J. Eakin, Y.Xie, R. Pelcovits, M. Radcliffe, and G. Crawford, Appl. Phys. Lett. **85**, 1671 (2004).

[20] S. Gorkhali, Ph.D. thesis, Brown University (2007).

[21] B. S. Murray, R. A. Pelcovits, and C. Rosenblatt, Phys. Rev. E **90**, 052501 (2014).

[22] P. Kaiser, W. Wiese, and S. Hess, J. Non-Equilib. Thermodyn. **17**, 153 (1992).

[23] P. G. de Gennes and J. Prost, *The Physics of Liquid Crystals* (Oxford University Press, Oxford, 1993).

[24] M. Nobili and G. Durand, Phys. Rev. A **46**, R6174 (1992).

[25] S. Kralj, E. G. Virga, and S. Žumer, Phys. Rev. E **60**, 1858 (1999).

[26] F. Bisi, E. C. Gartland, R. Rosso, and E. G. Virga, Phys. Rev.. E **68**, 021707 (2003).

[27] N. Schopohl and T. J. Sluckin, Phys. Rev. Lett. **59**, 2582 (1987).

[28] R. Hamdi, G. Lombardo, M. de Santo, and R. Barberi, Eur. Phys. J. E **36**, 115 (2013).

[29] E. Penzenstadler and H. R. Trebin, J. Phys. (France) **50**, 1025 (1989).

[30] N. Schopohl and T. J. Sluckin, J. Phys. (France) **49**, 1097 (1988).

[31] S. Kralj, S. Žumer, and D. W. Allender, Phys. Rev. A **43**, 2943 (1991).

[32] R. Rosso and E. G. Virga, J. Phys. A: Math. Gen. **29**, 4247 (1996).

[33] O. D. Lavrentovich and Y. A. Nastishin, Europhys. Lett. **12**, 135 (1990).

[34] P. Poulin and D. A. Weitz, Phys. Rev. E **57**, 626 (1998).

[35] V. Vitelli and A. M. Turner, Phys. Rev. Lett. **94**, 215301 (2004).

[36] M. Bowick, D. Nelson, and A. Travesset, Phys. Rev. E **69**, 041102 (2004).

[37] D. Jesenek, S. Kralj, R. Rosso, and E. Virga, Soft Matter **11**, 24342444 (2015).

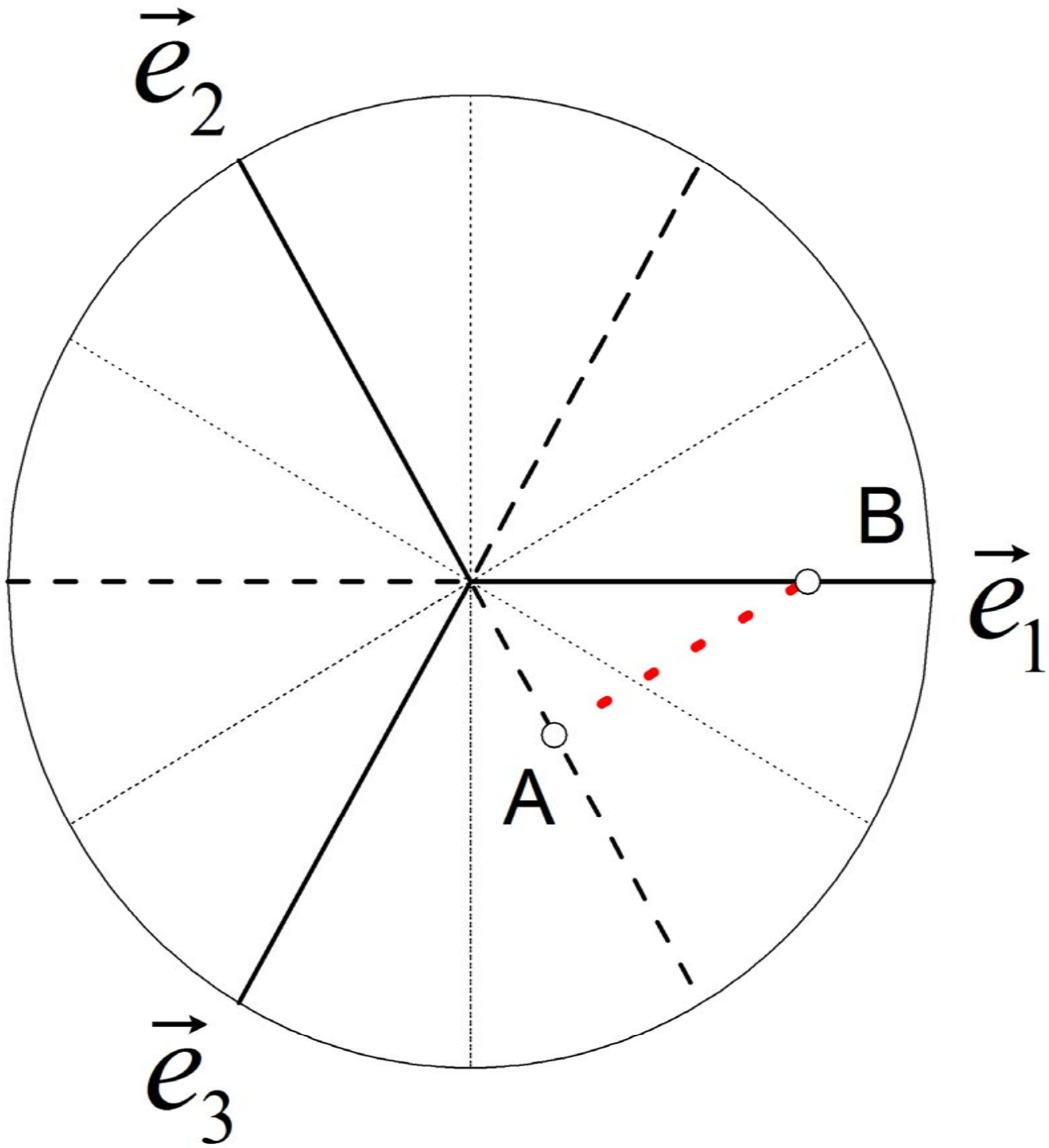
$\vec{e}_2$
B
$\vec{e}_1$
A
$\vec{e}_3$

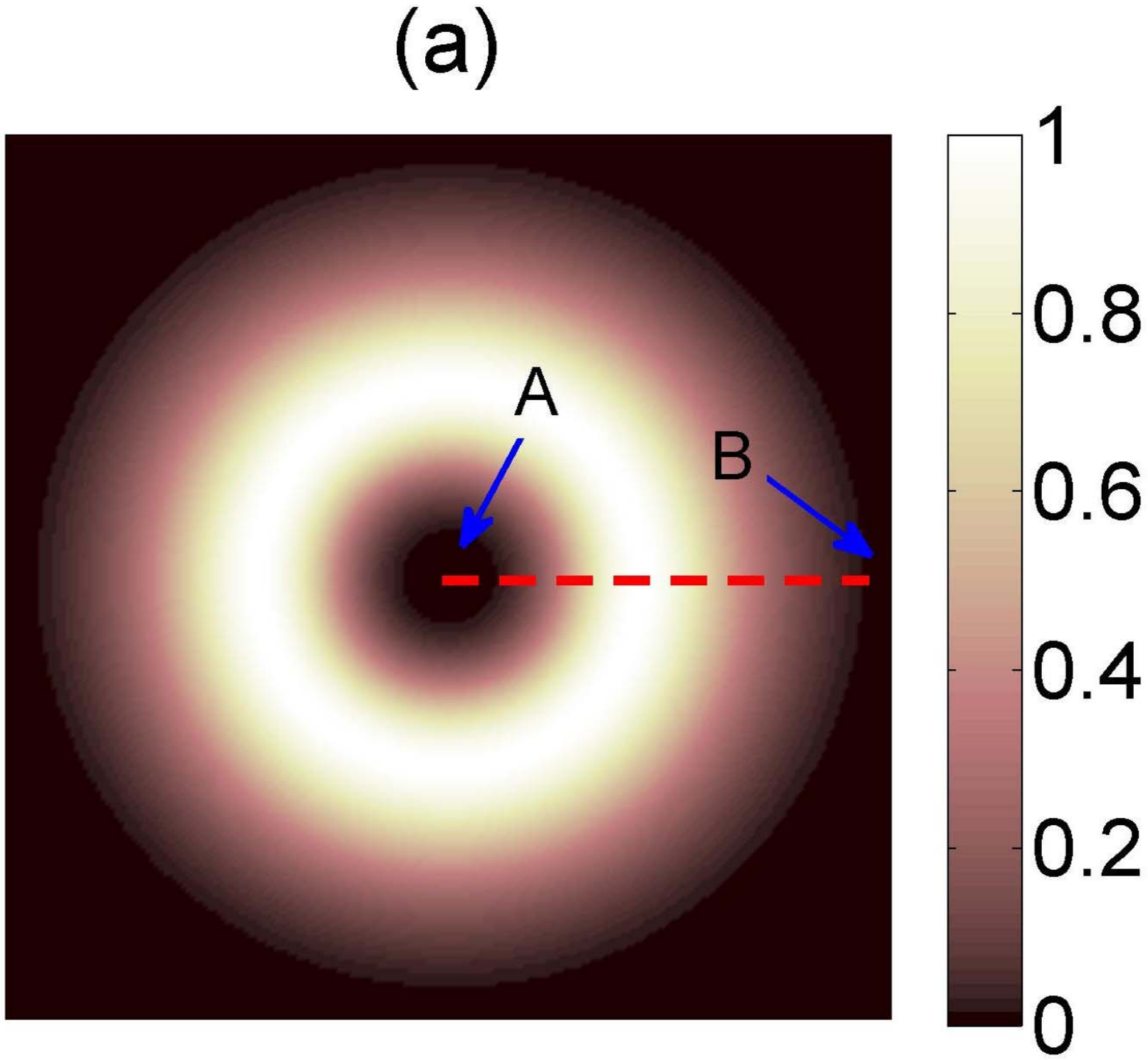
(a)
A
B
1
0.8
0.6
0.4
0.2
0

(b)

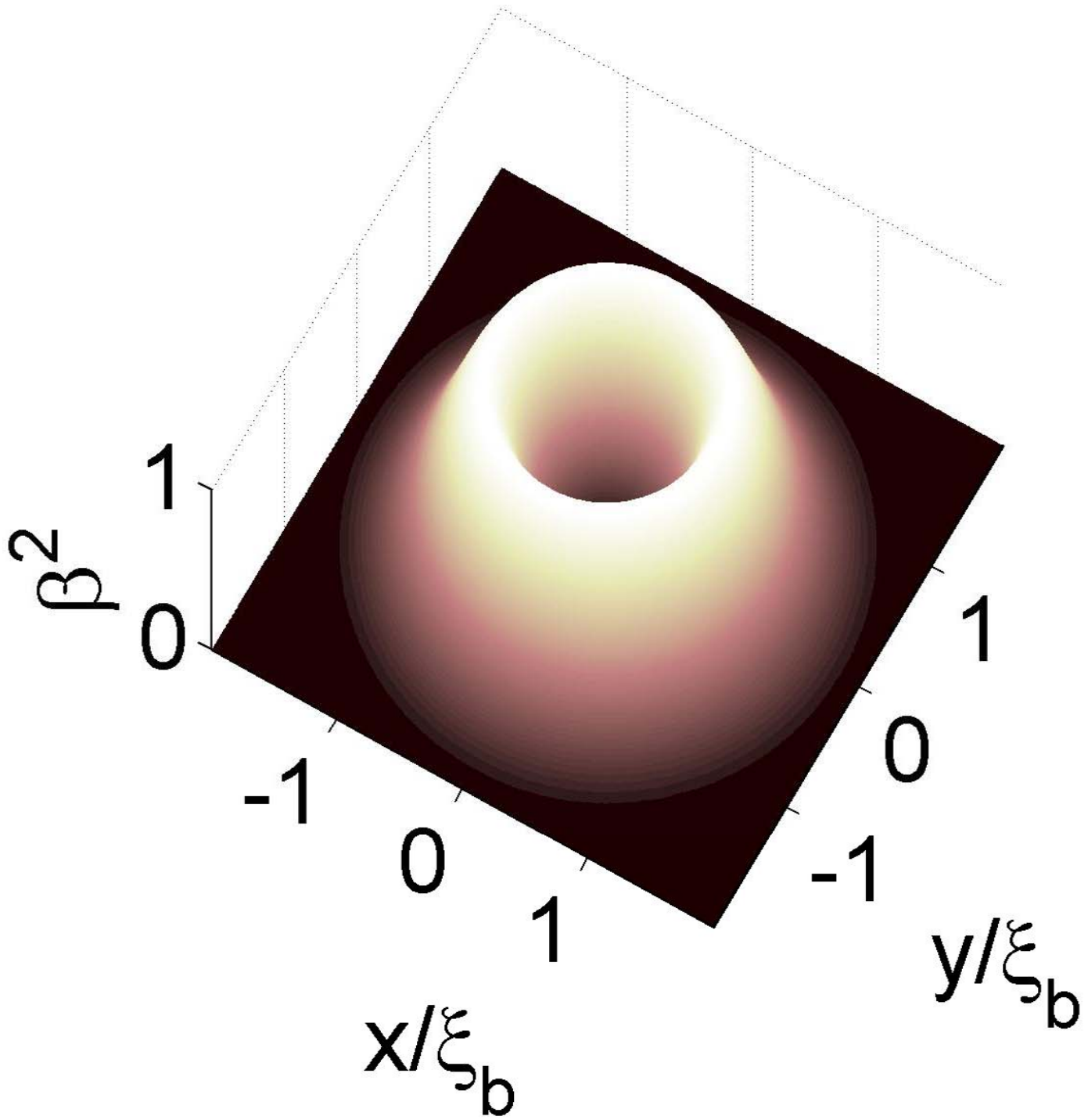

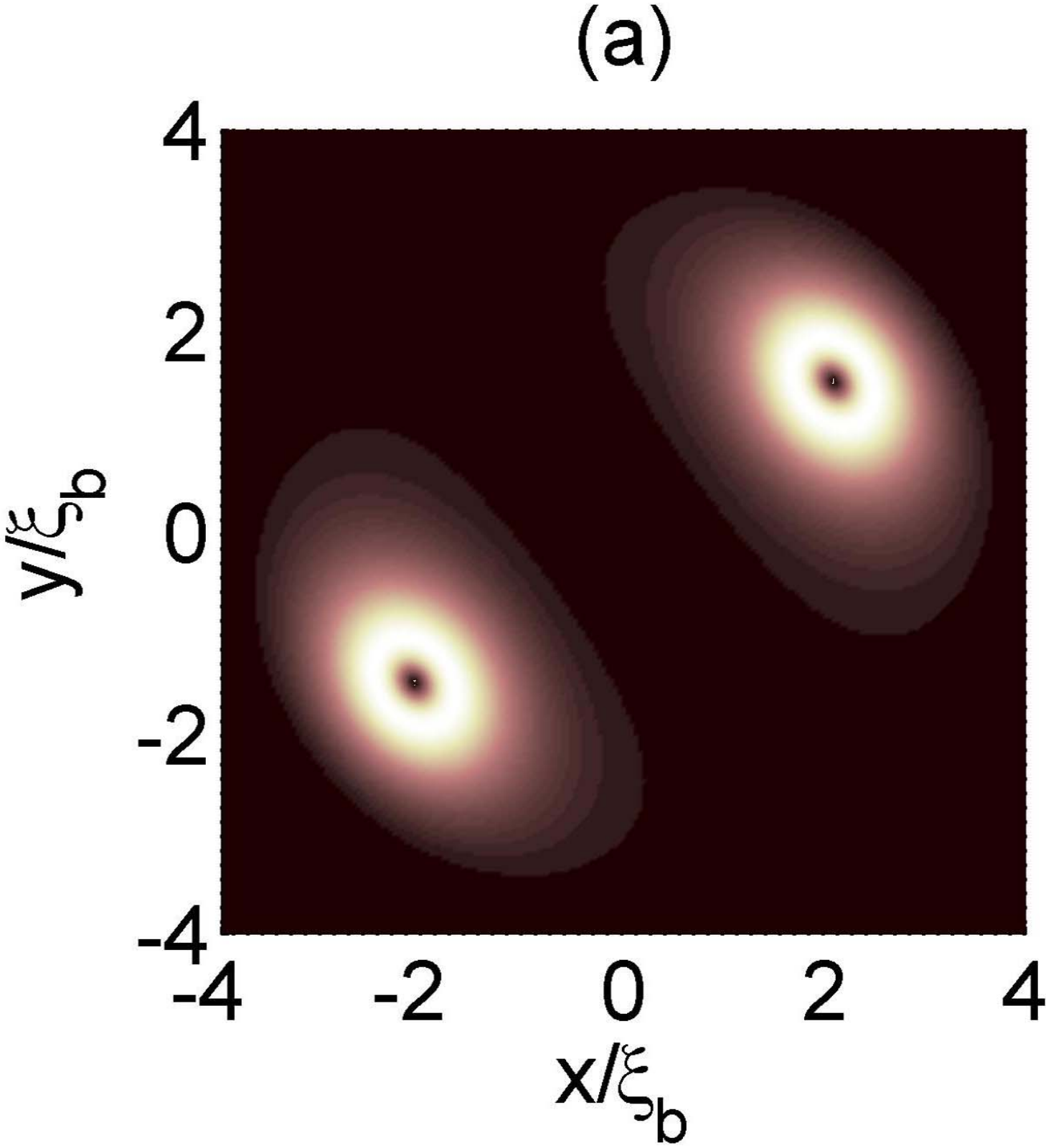
(a)
4
2
0
-2
-4
y/ξb
-4
-2
0
2
4
x/ξb

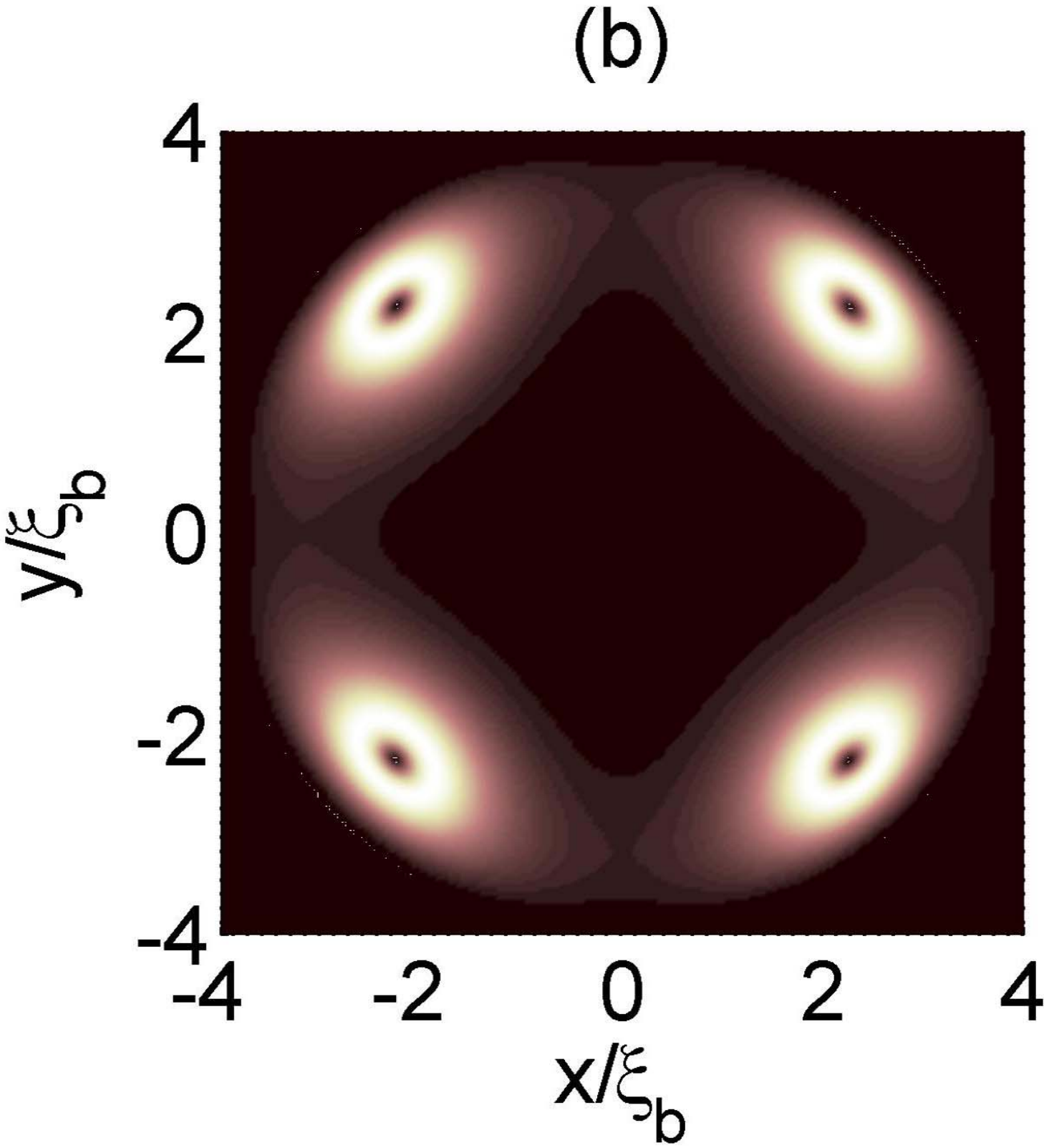
(b)
4
2
0
-2
-4
y/ξb
-4
-2
0
2
4
x/ξb

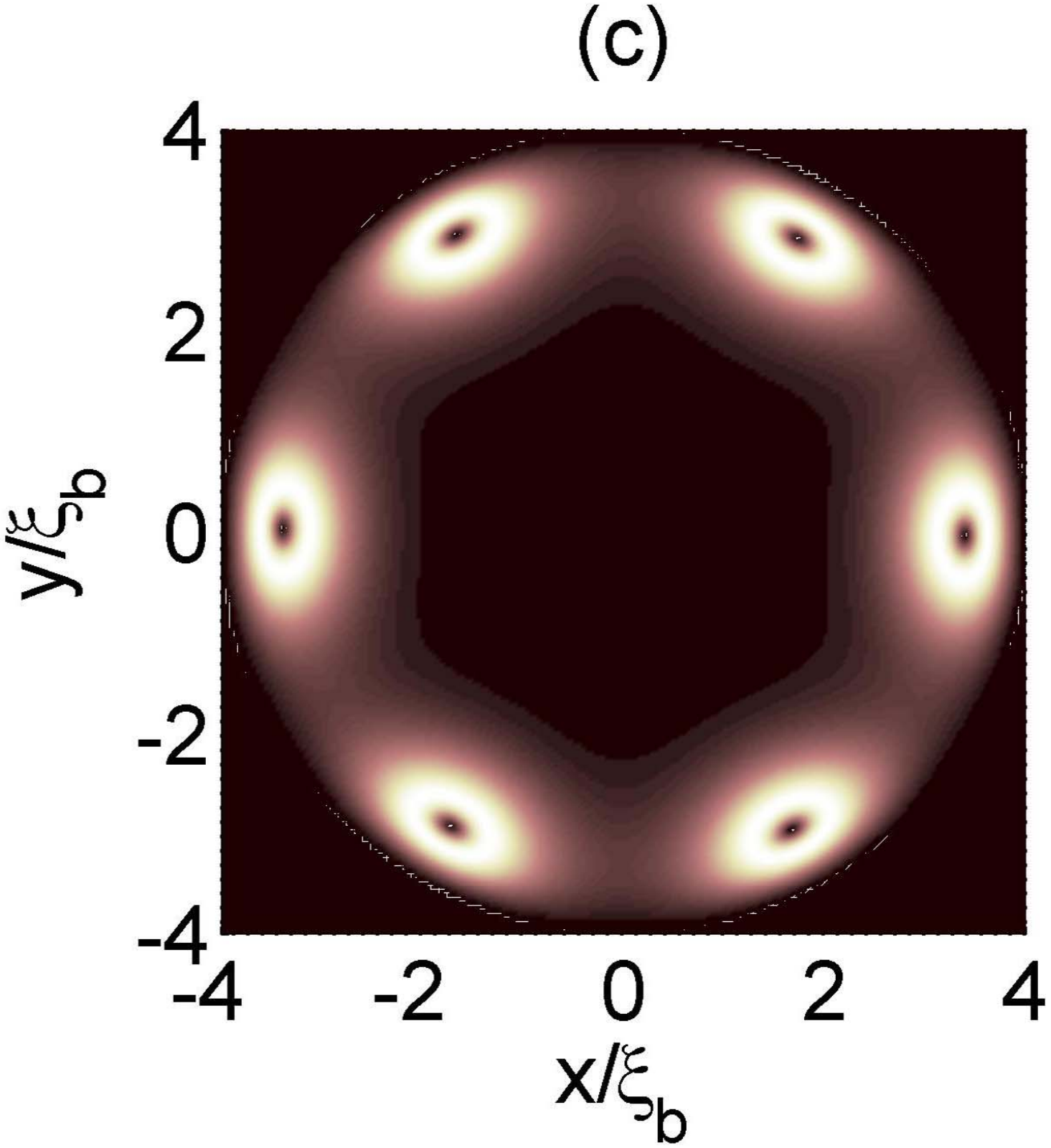
(c)
4
2
0
-2
-4
y/ξb
-4
-2
0
2
4
x/ξb

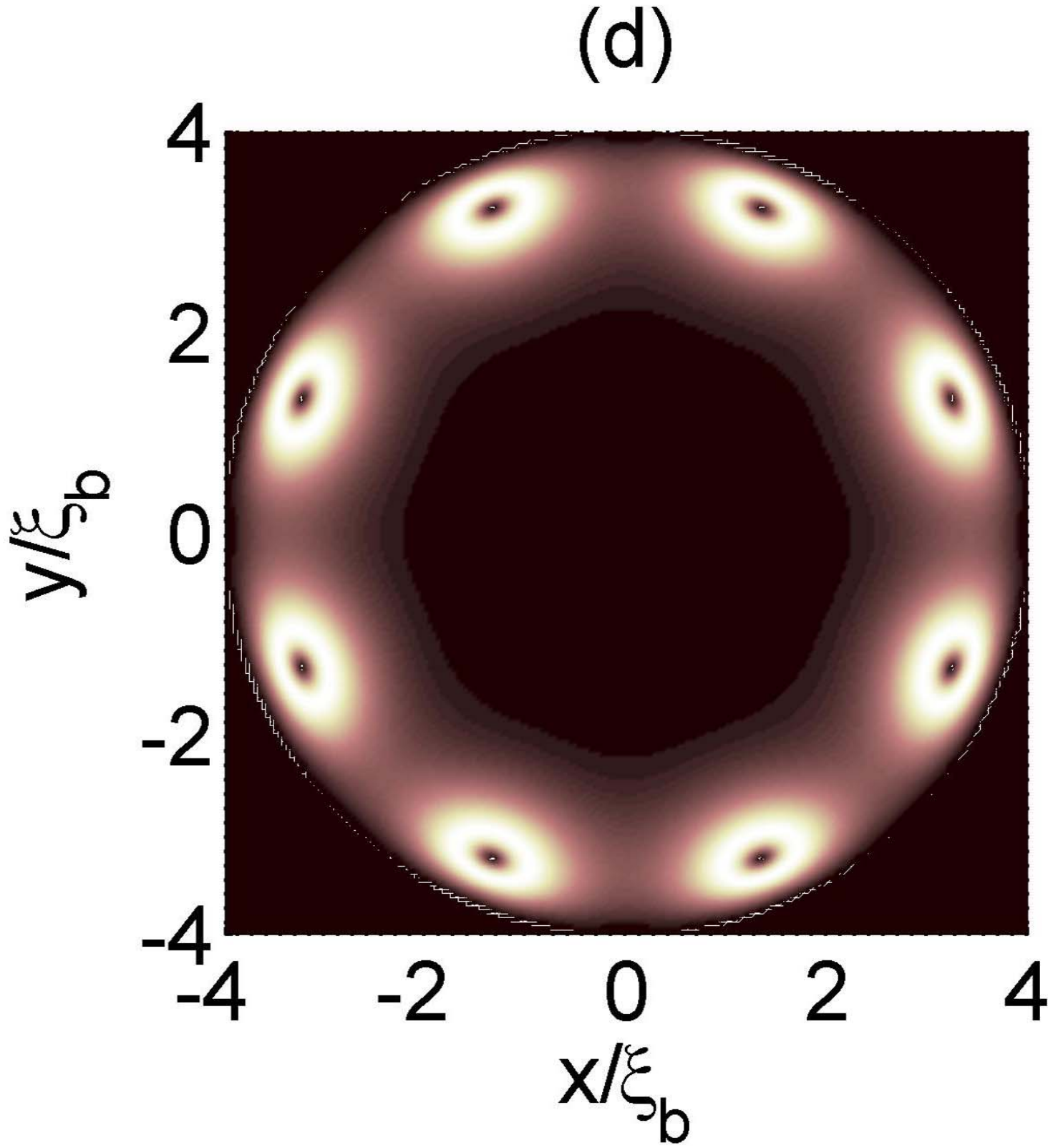
(d)
4
2
0
-2
-4
y/ξb
-4
-2
0
2
4
x/ξb

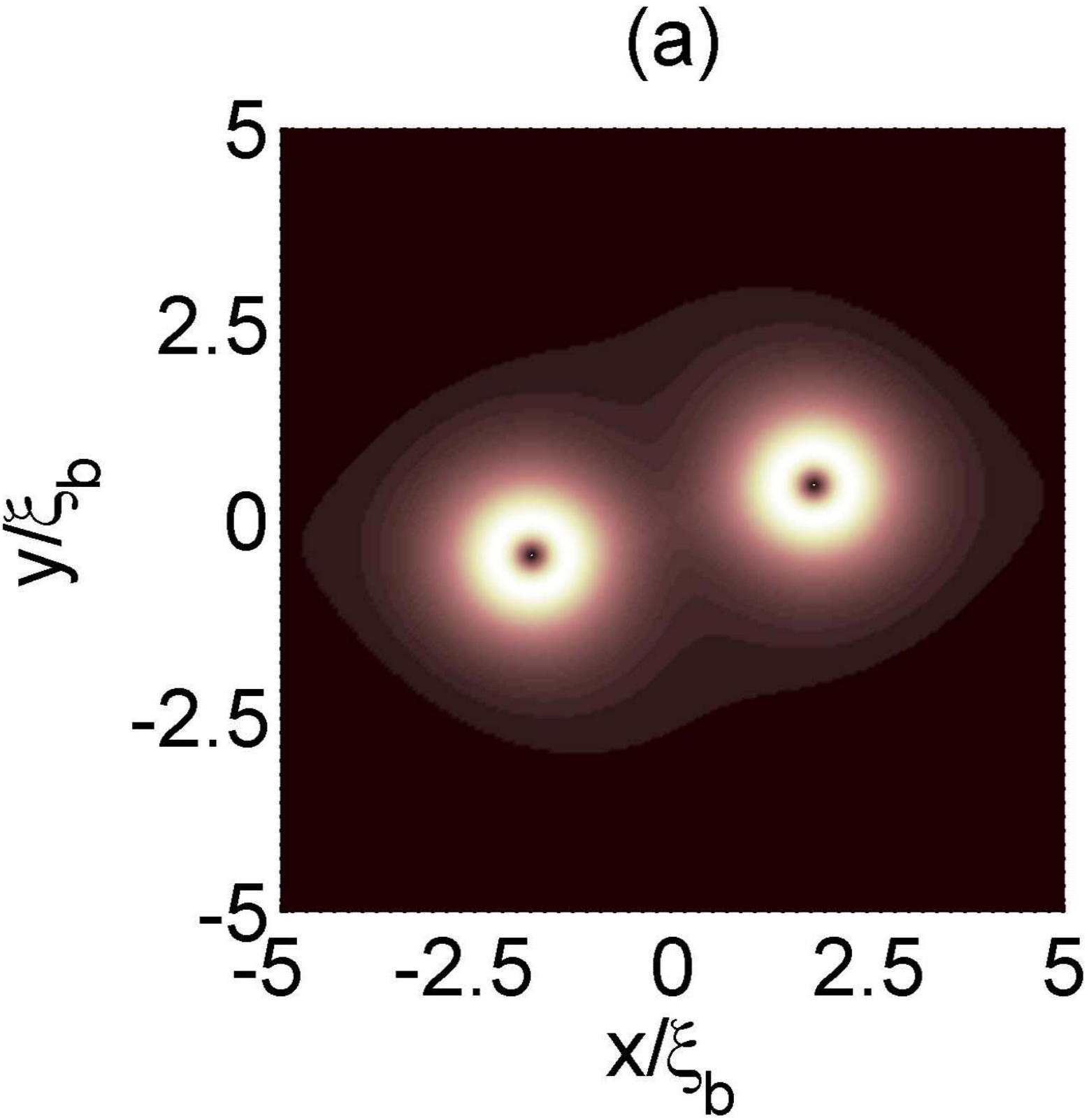
(a)
5
2.5
0
-2.5
-5
y/ξb
-5
-2.5
0
2.5
5
x/ξb

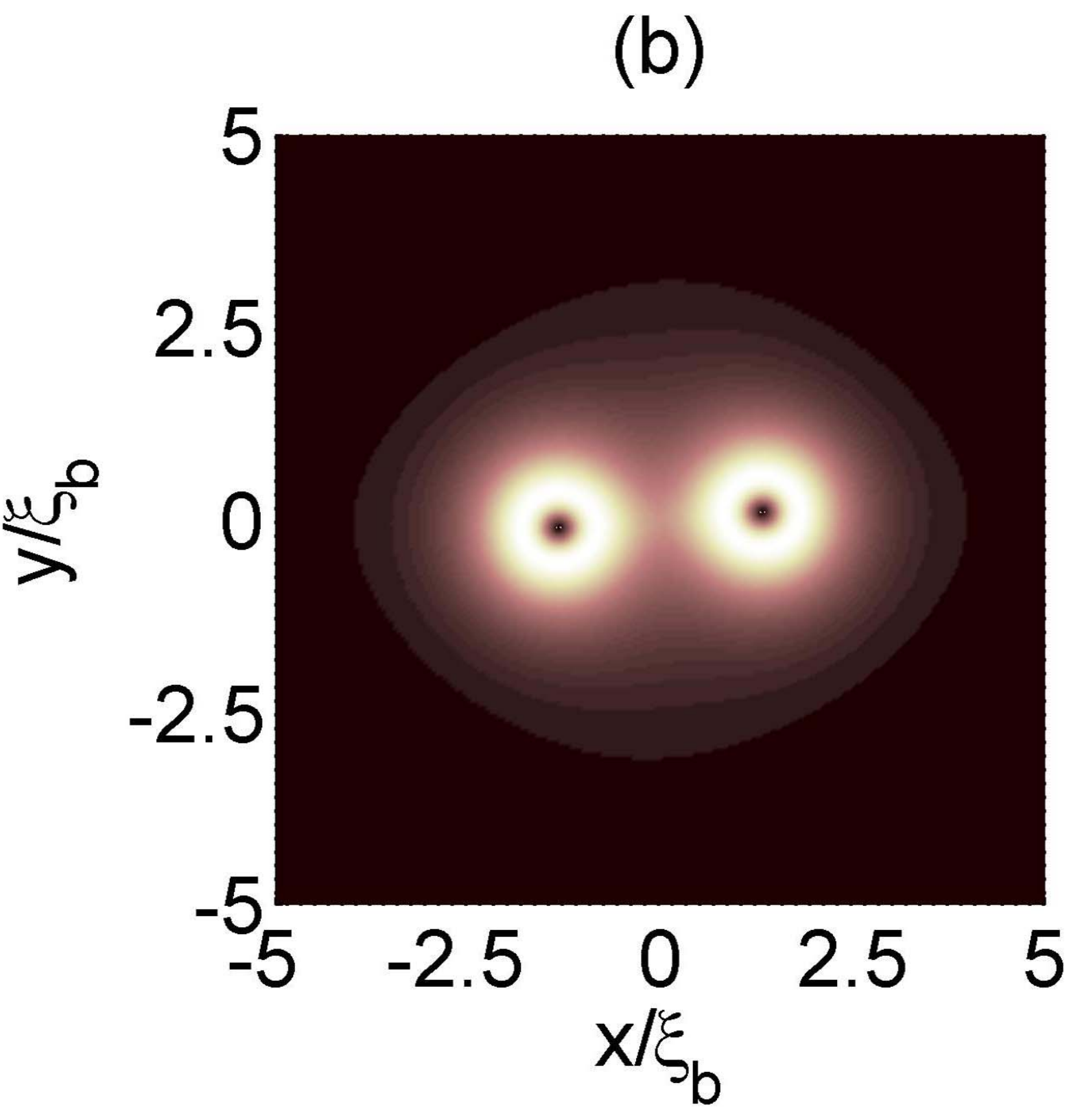
(b)
5
2.5
0
-2.5
-5
y/ξb
-5
-2.5
0
2.5
5
x/ξb

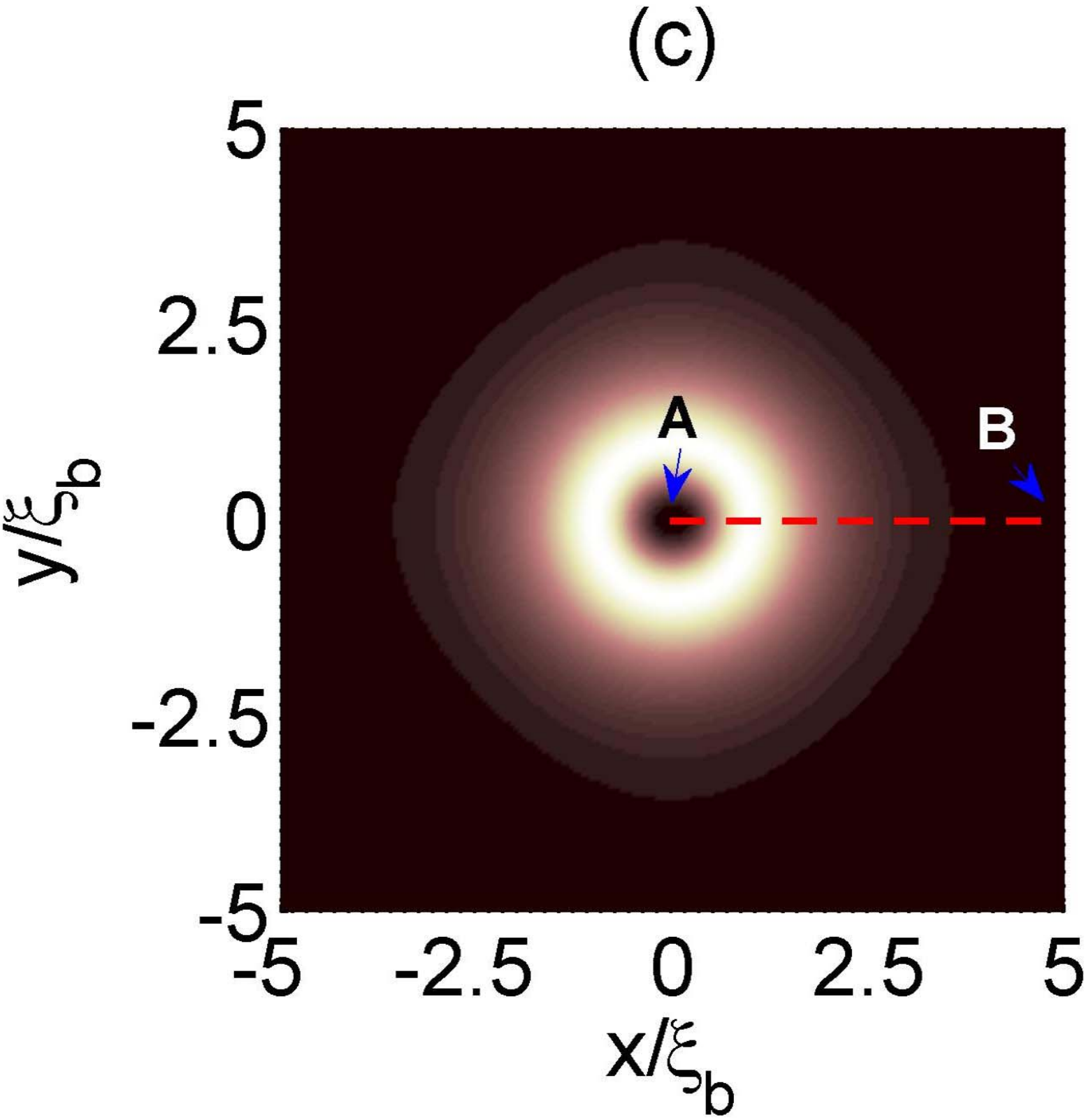
(c)
5
2.5
0
-2.5
-5
y/ξb
A
B
-5
-2.5
0
2.5
5
x/ξb

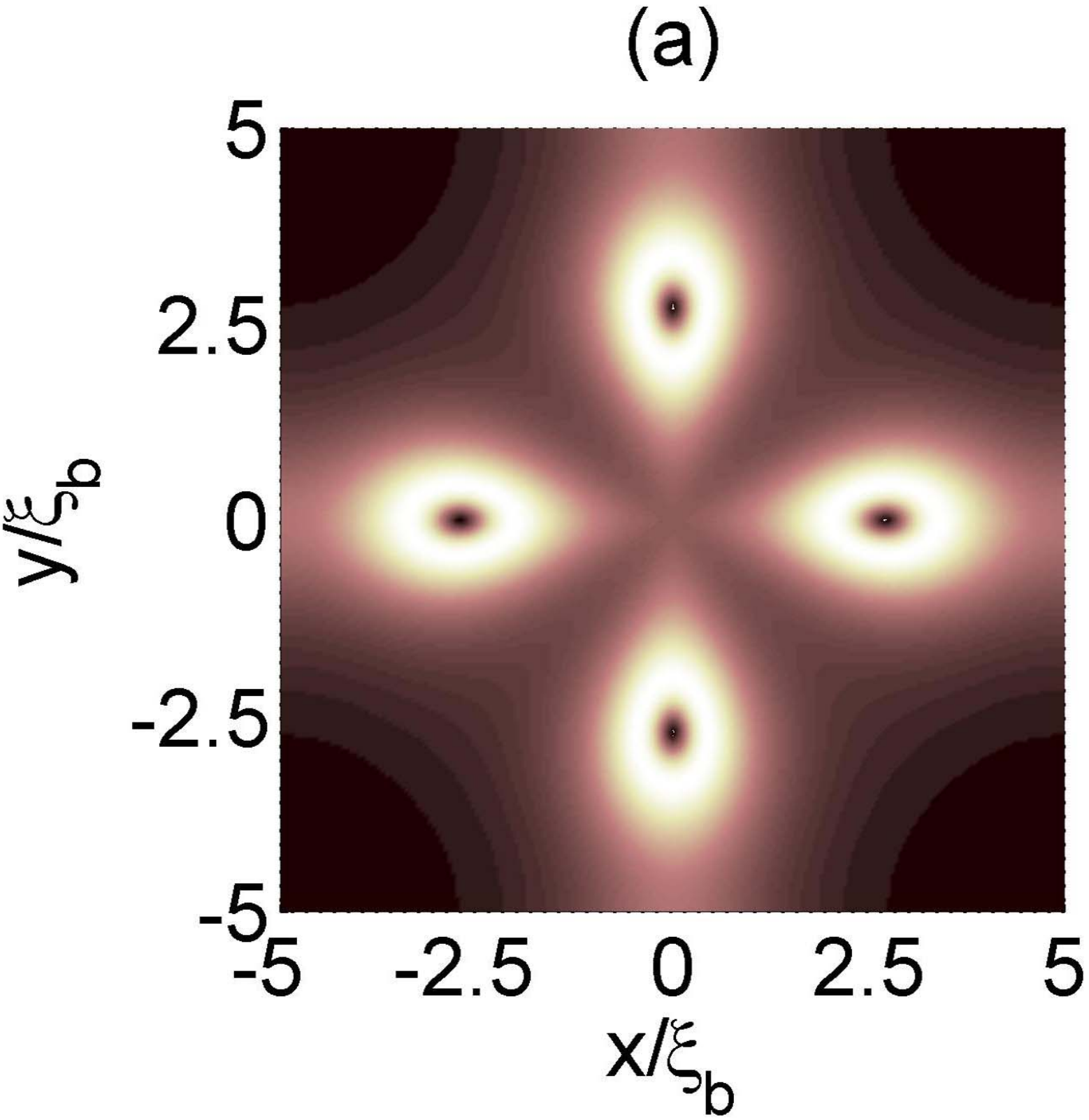
(a)
5
2.5
0
-2.5
-5
y/ξb
-5
-2.5
0
2.5
5
x/ξb

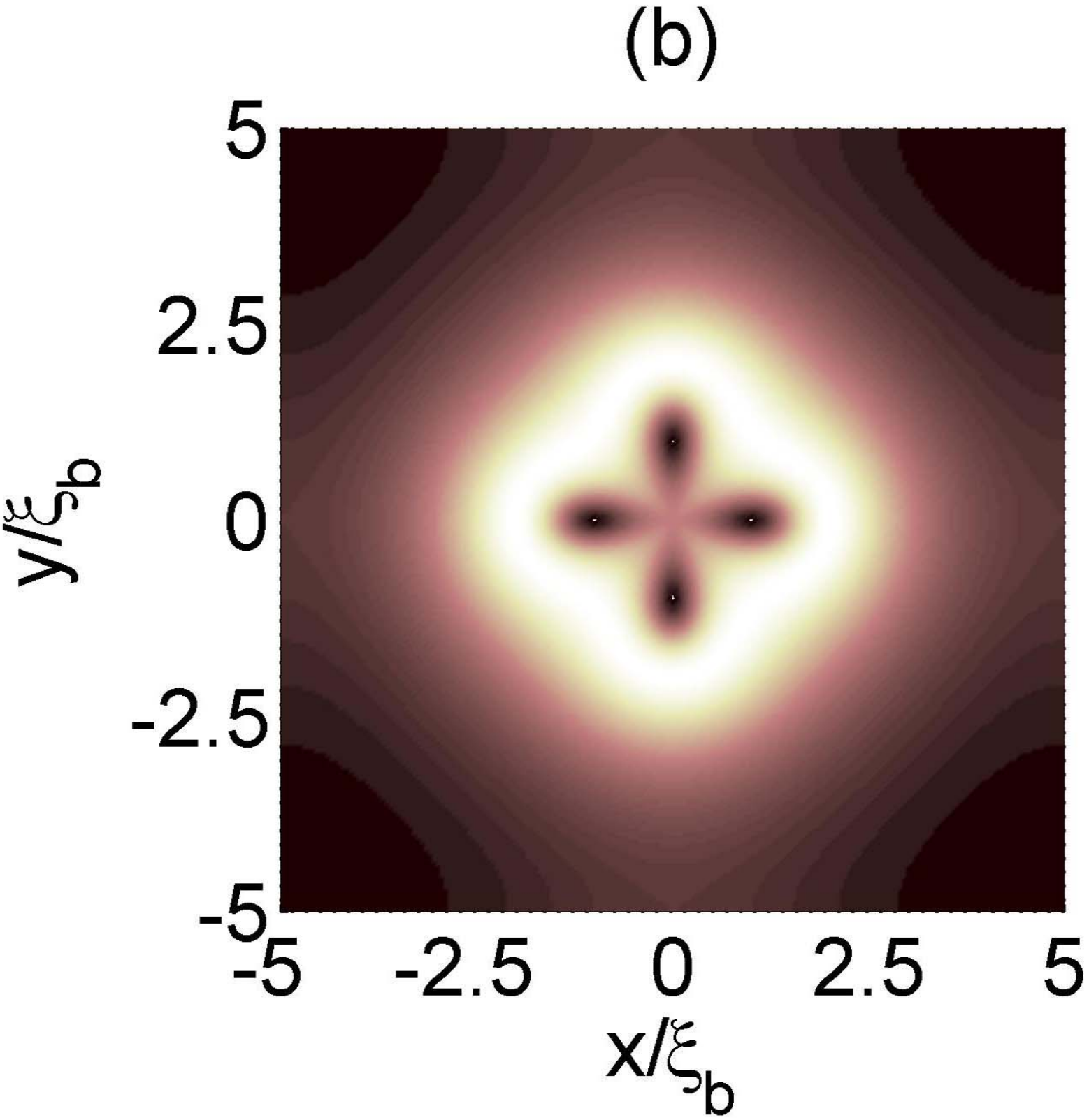
(b)
5
2.5
0
-2.5
-5
y/ξb
-5
-2.5
0
2.5
5
x/ξb

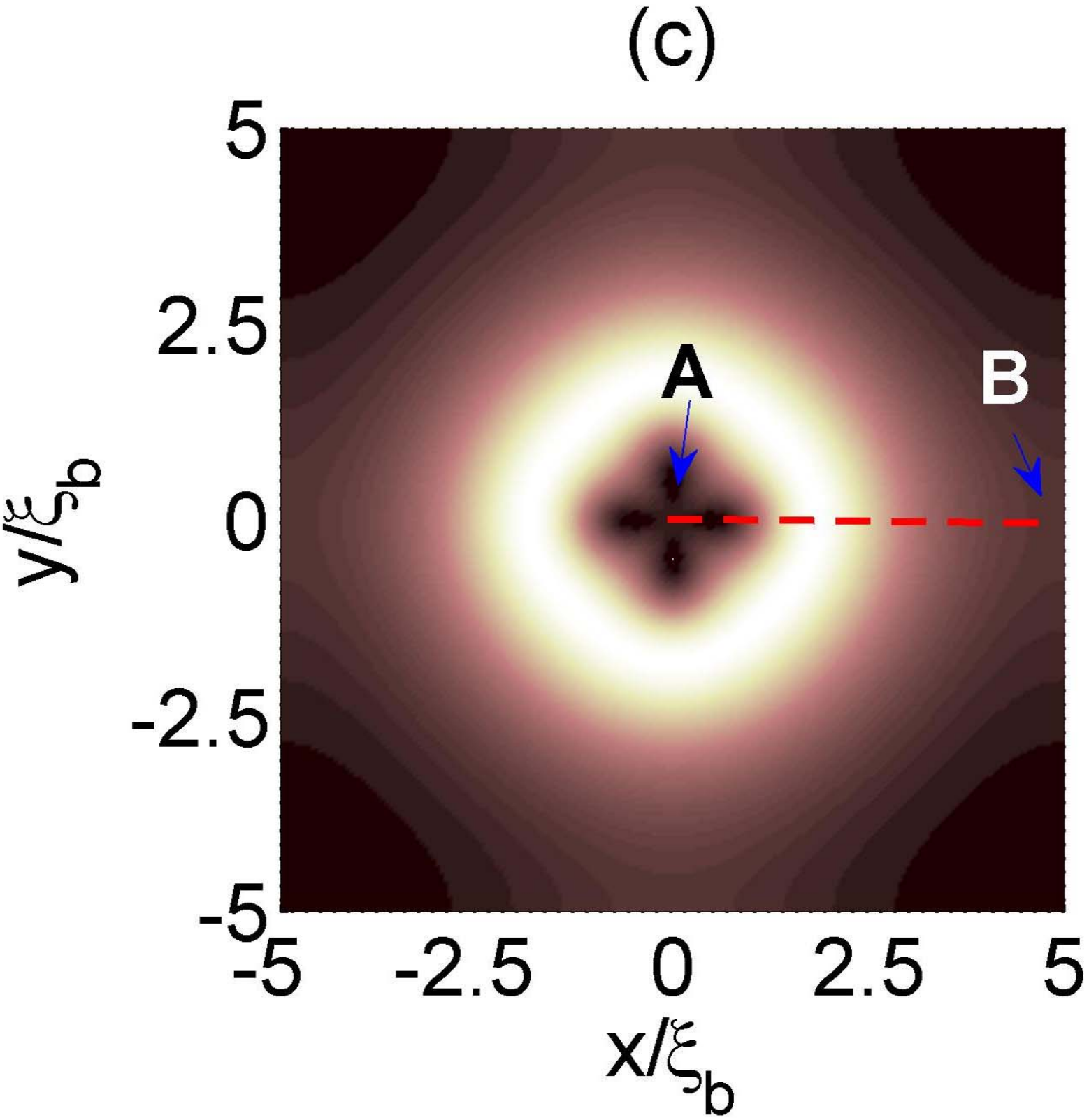
(c)
5
2.5
0
-2.5
-5
A
B
y/ξb
-5
-2.5
0
2.5
5
x/ξb

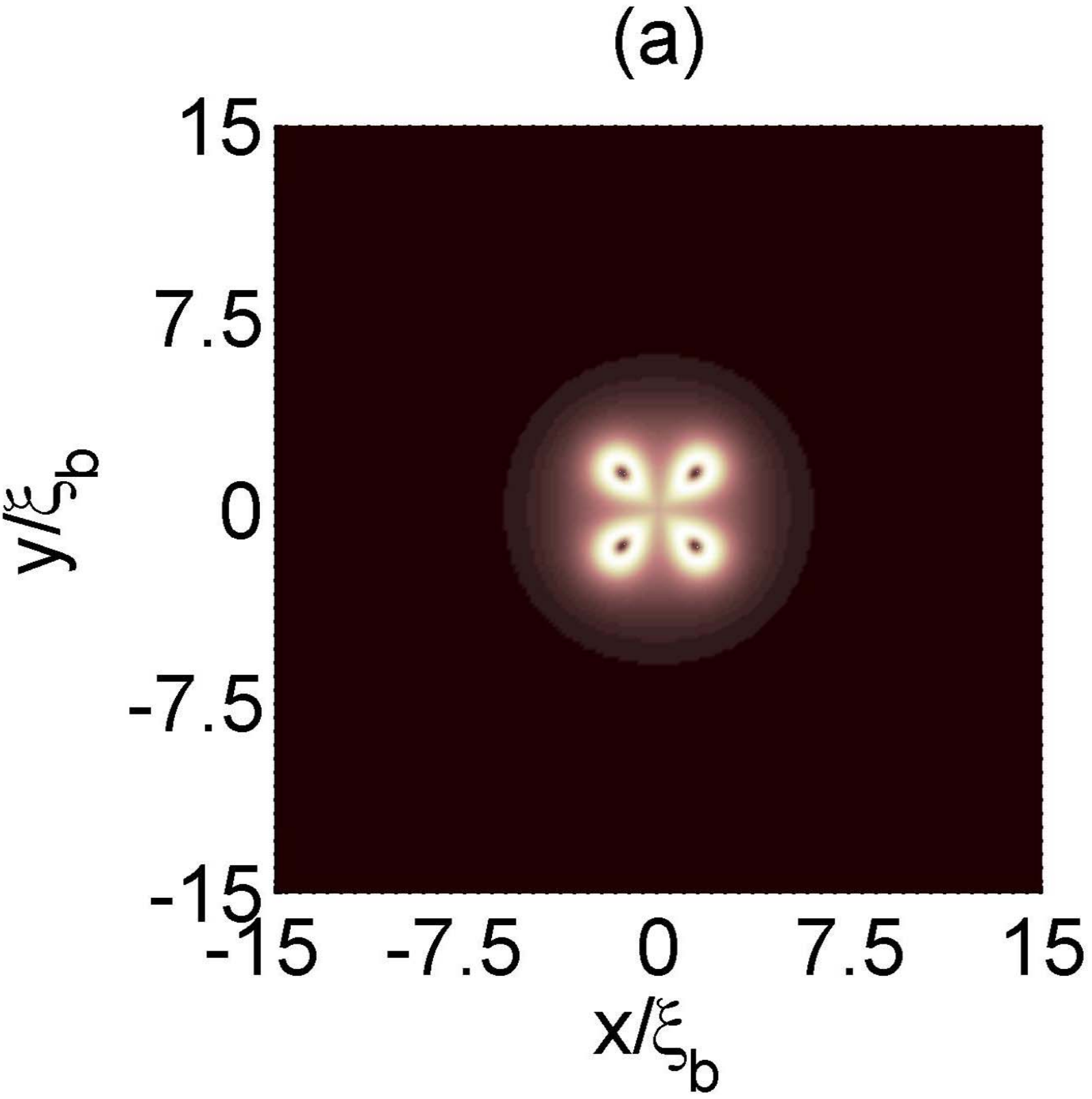
(a)
15
7.5
0
-7.5
-15
y/ξb
-15
-7.5
0
7.5
15
x/ξb

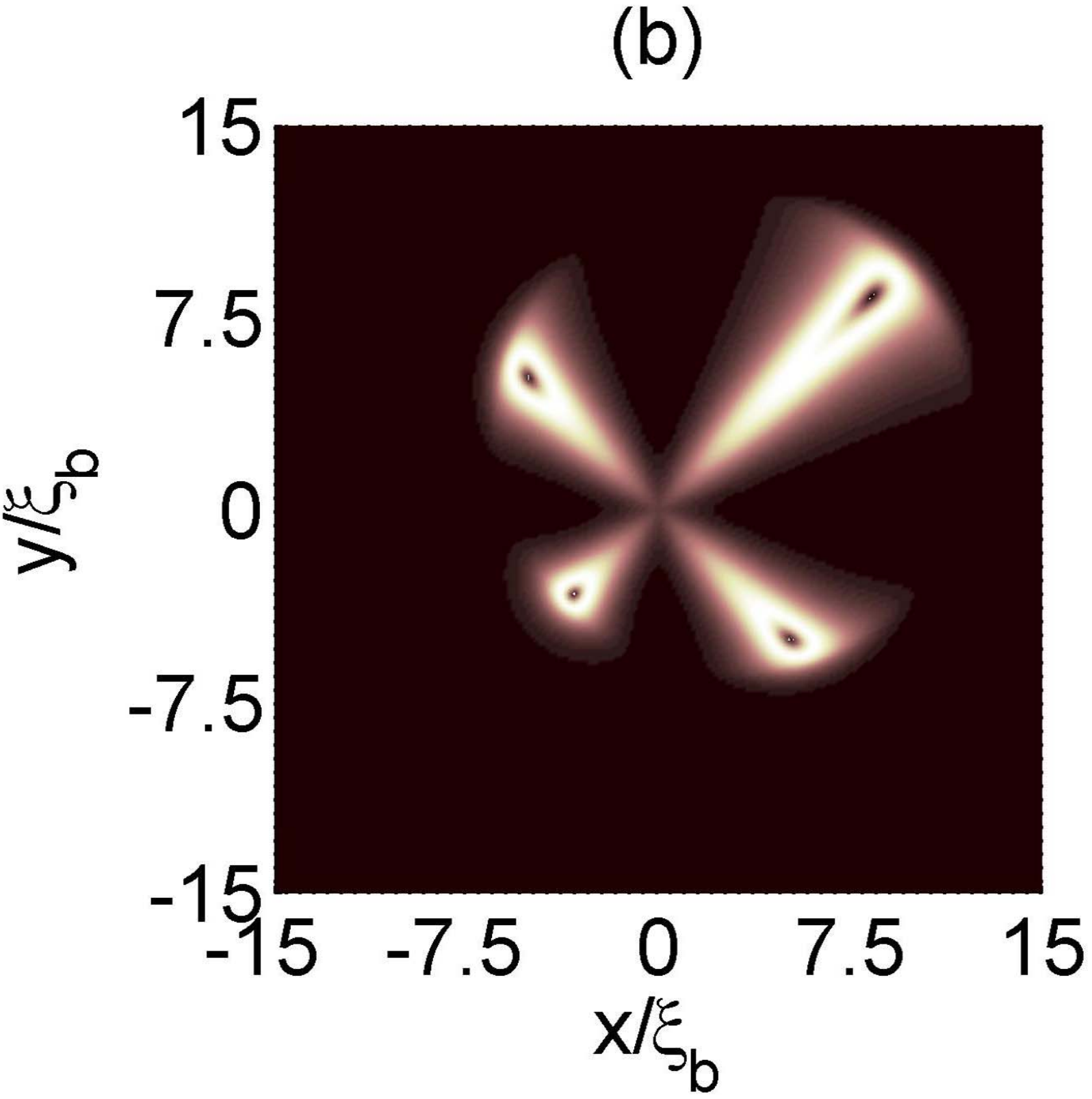
(b)
15
7.5
0
-7.5
-15
y/ξb
-15
-7.5
0
7.5
15
x/ξb

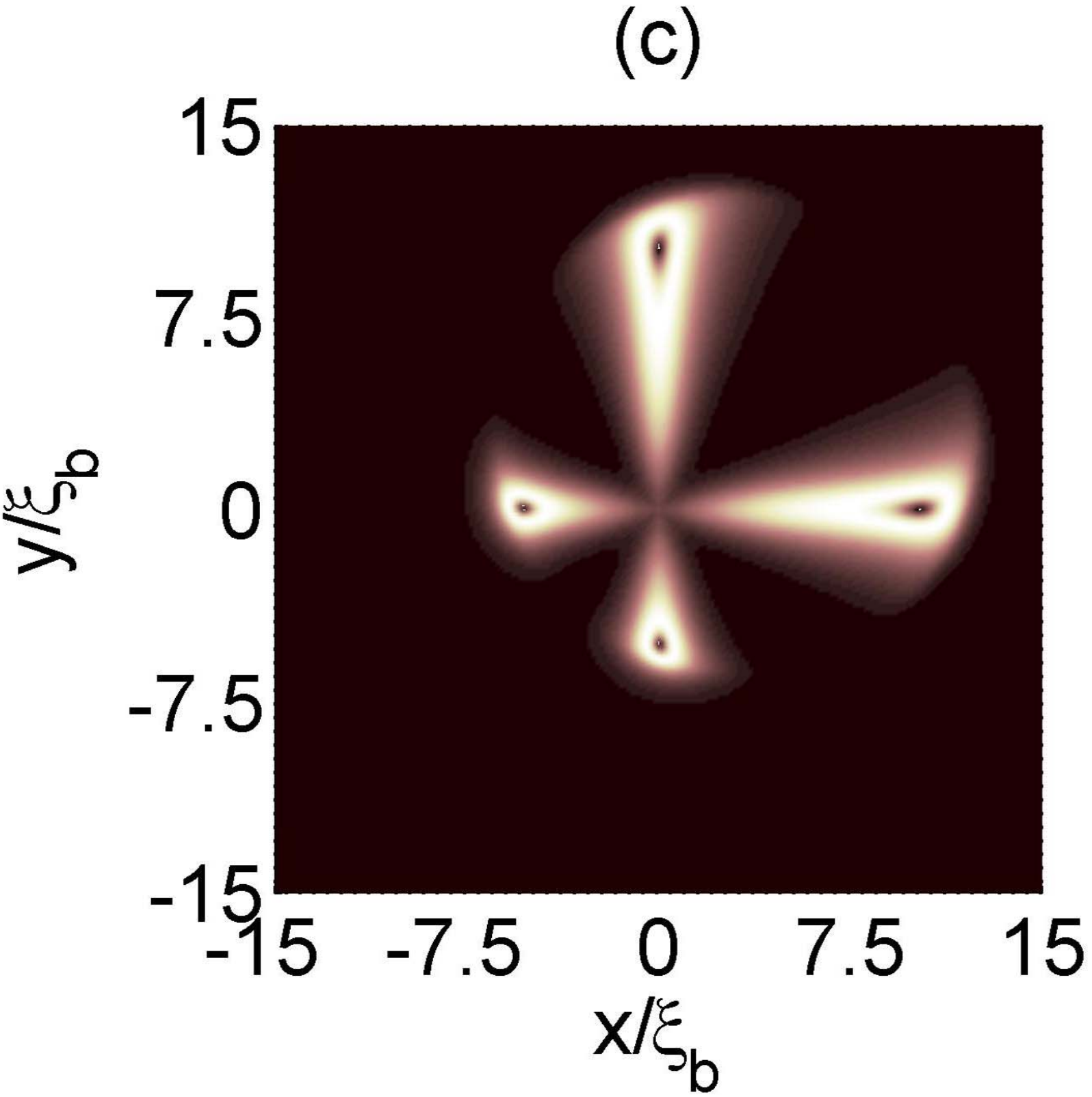
(c)
15
7.5
0
-7.5
-15
y/ξb
-15
-7.5
0
7.5
15
x/ξb

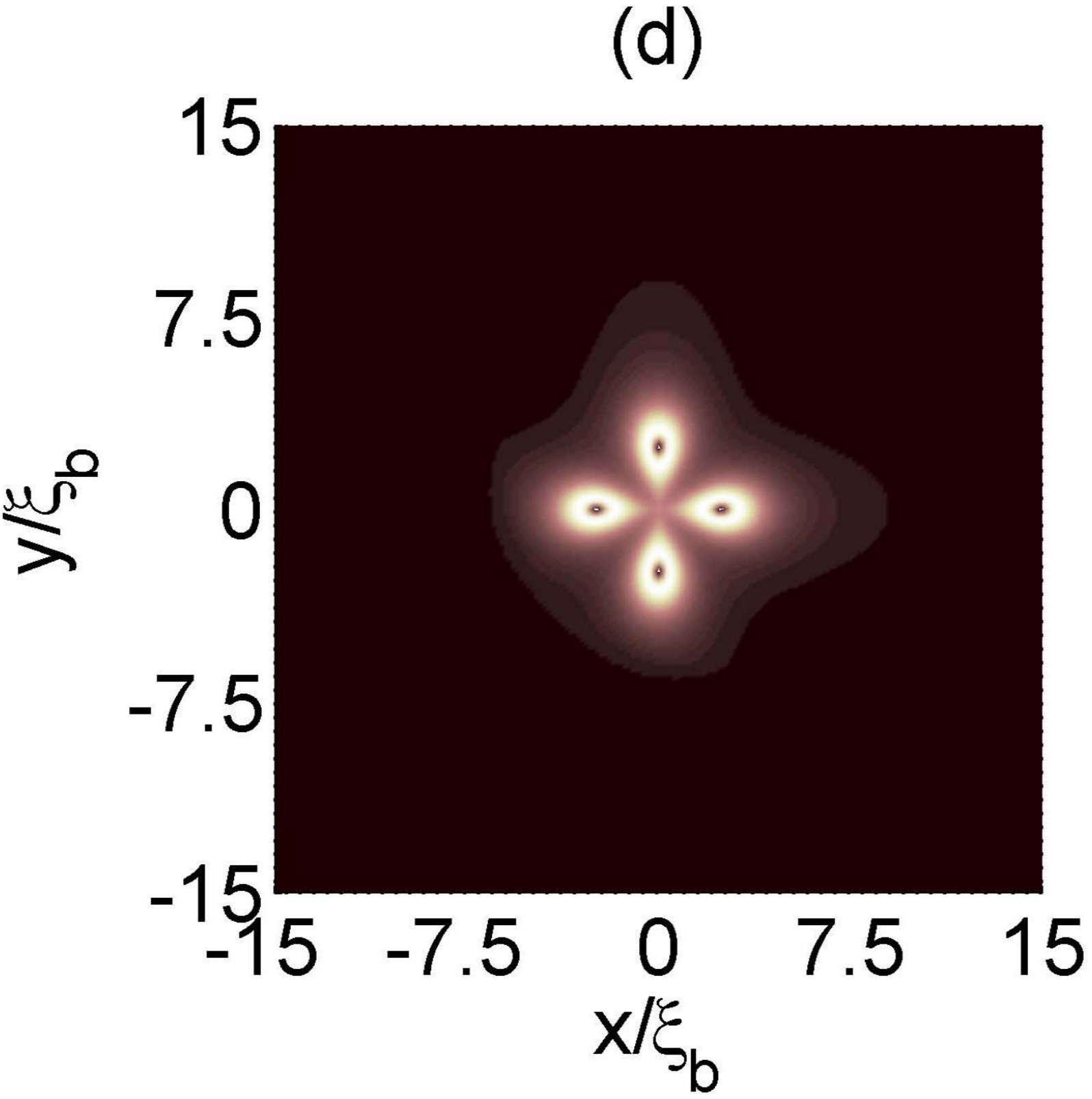
(d)
15
7.5
0
-7.5
-15
y/ξb
-15
-7.5
0
7.5
15
x/ξb

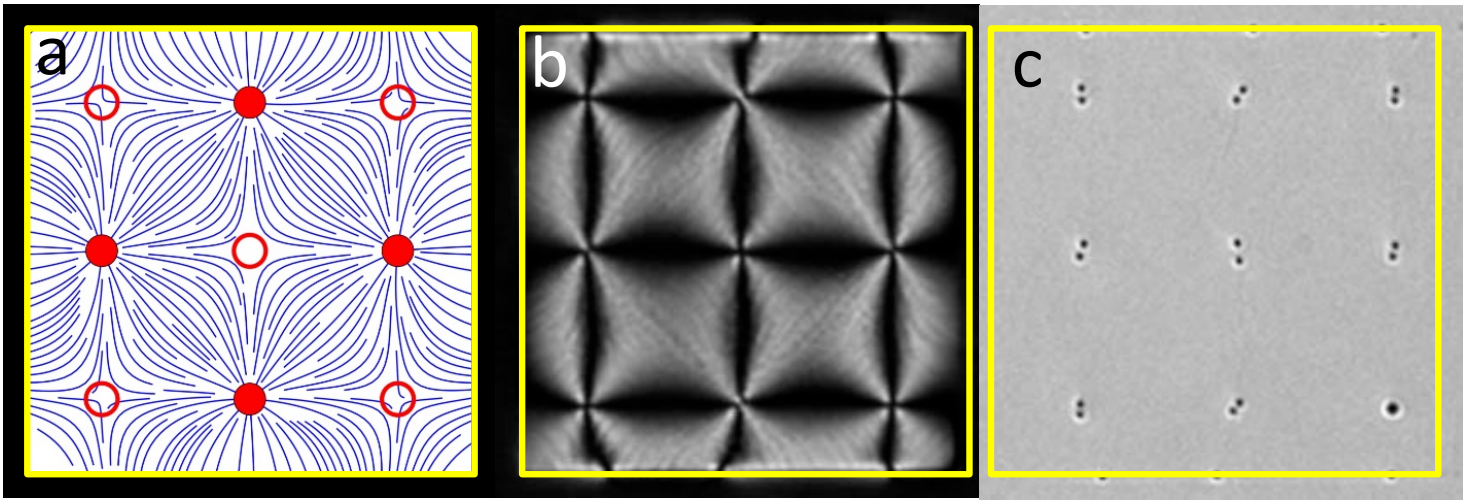
a
b
c

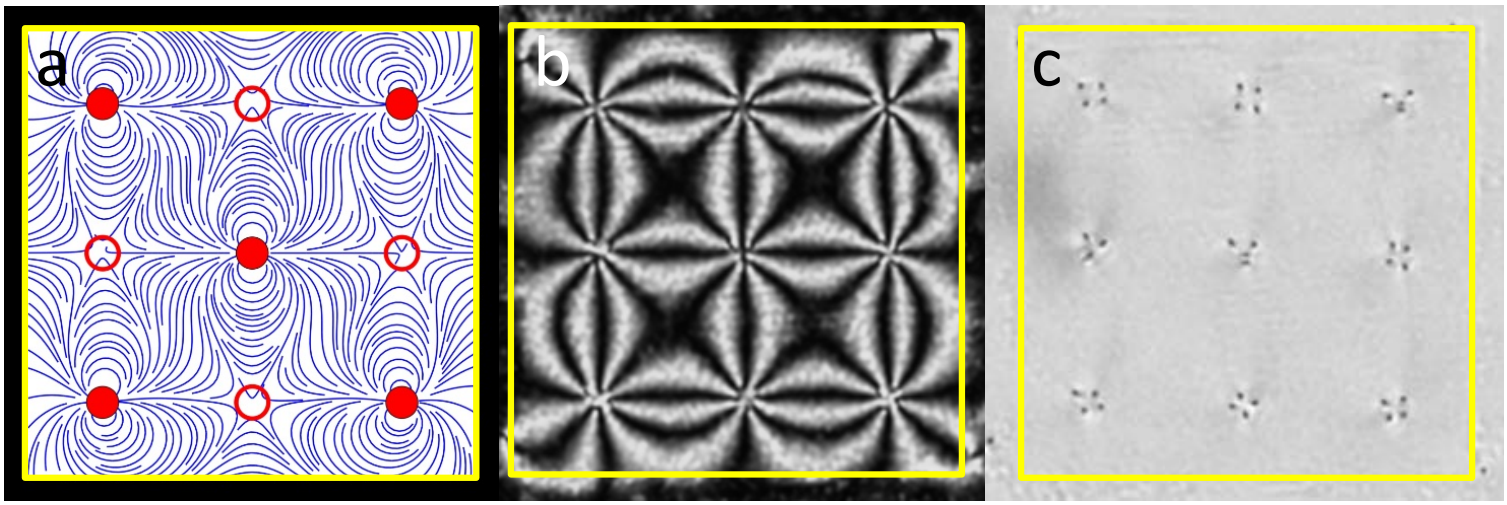
a
b
c

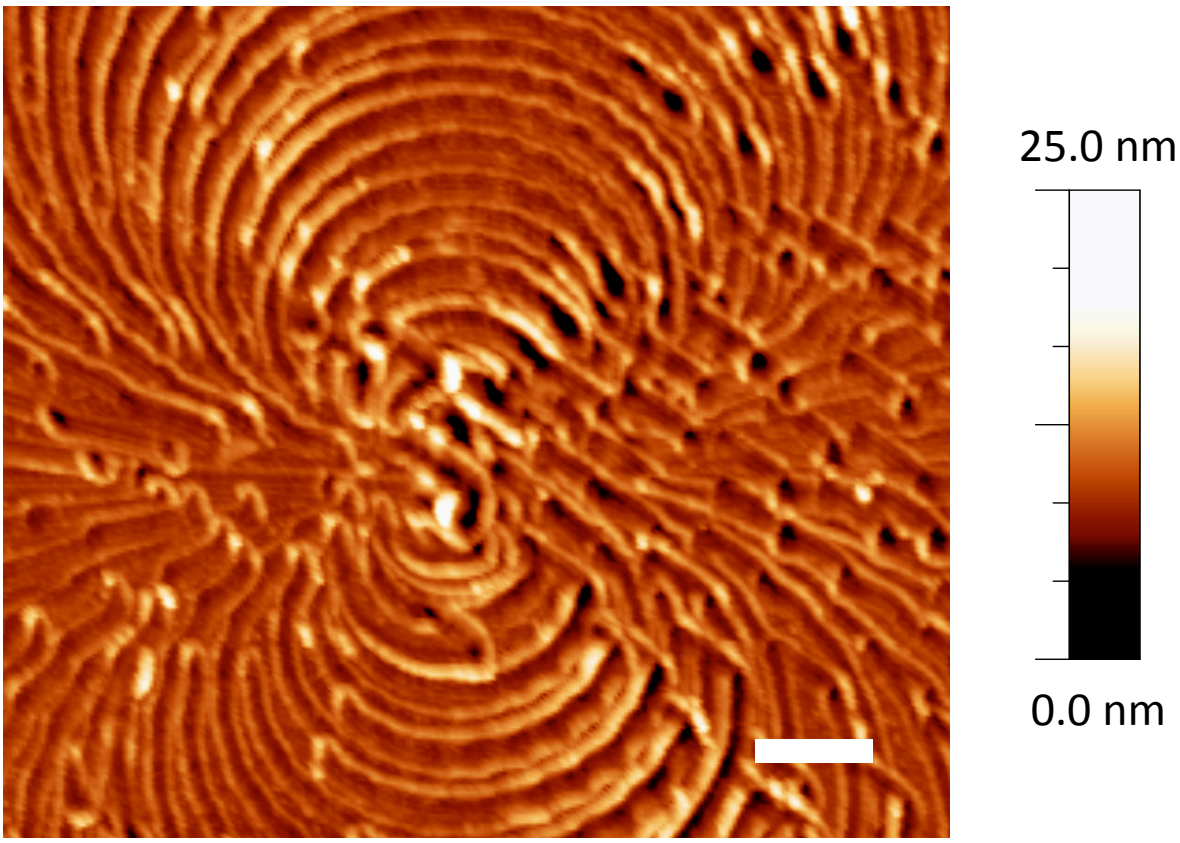
25.0 nm
0.0 nm

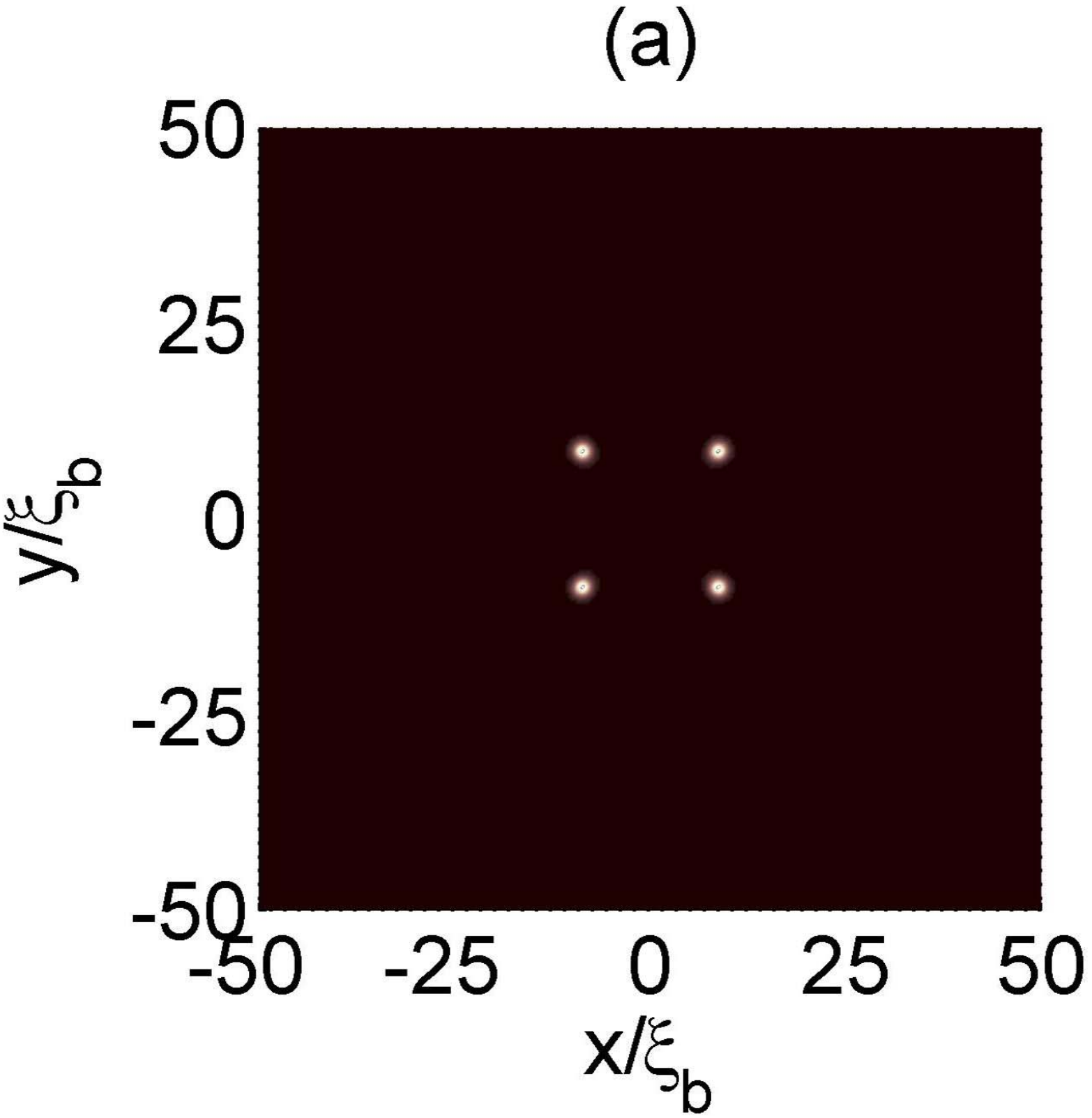
(a)
50
25
0
-25
-50
y/ξb
-50
-25
0
25
50
x/ξb

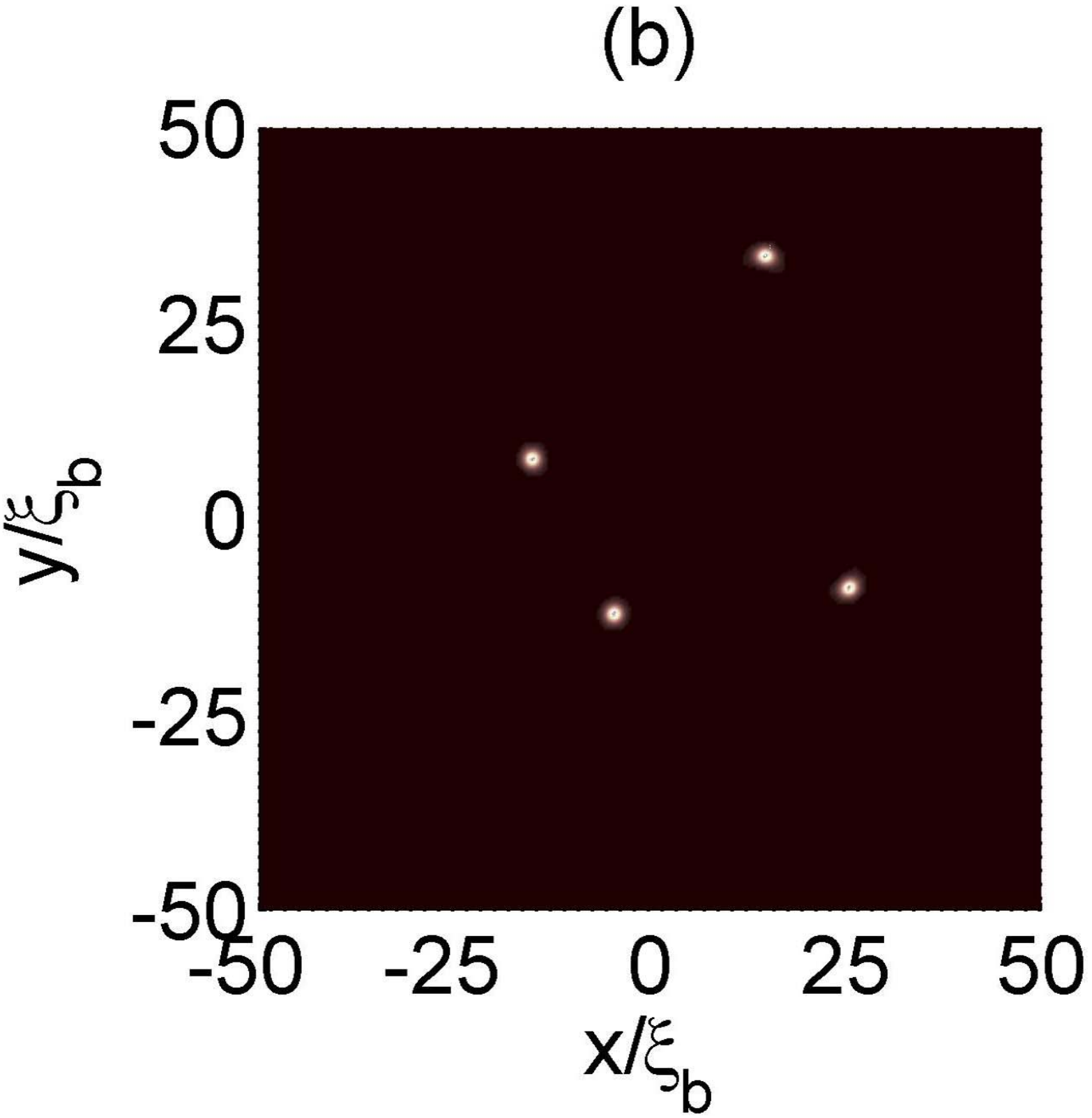
(b)
50
25
0
-25
-50
-50
-25
0
25
50
y/ξb
x/ξb

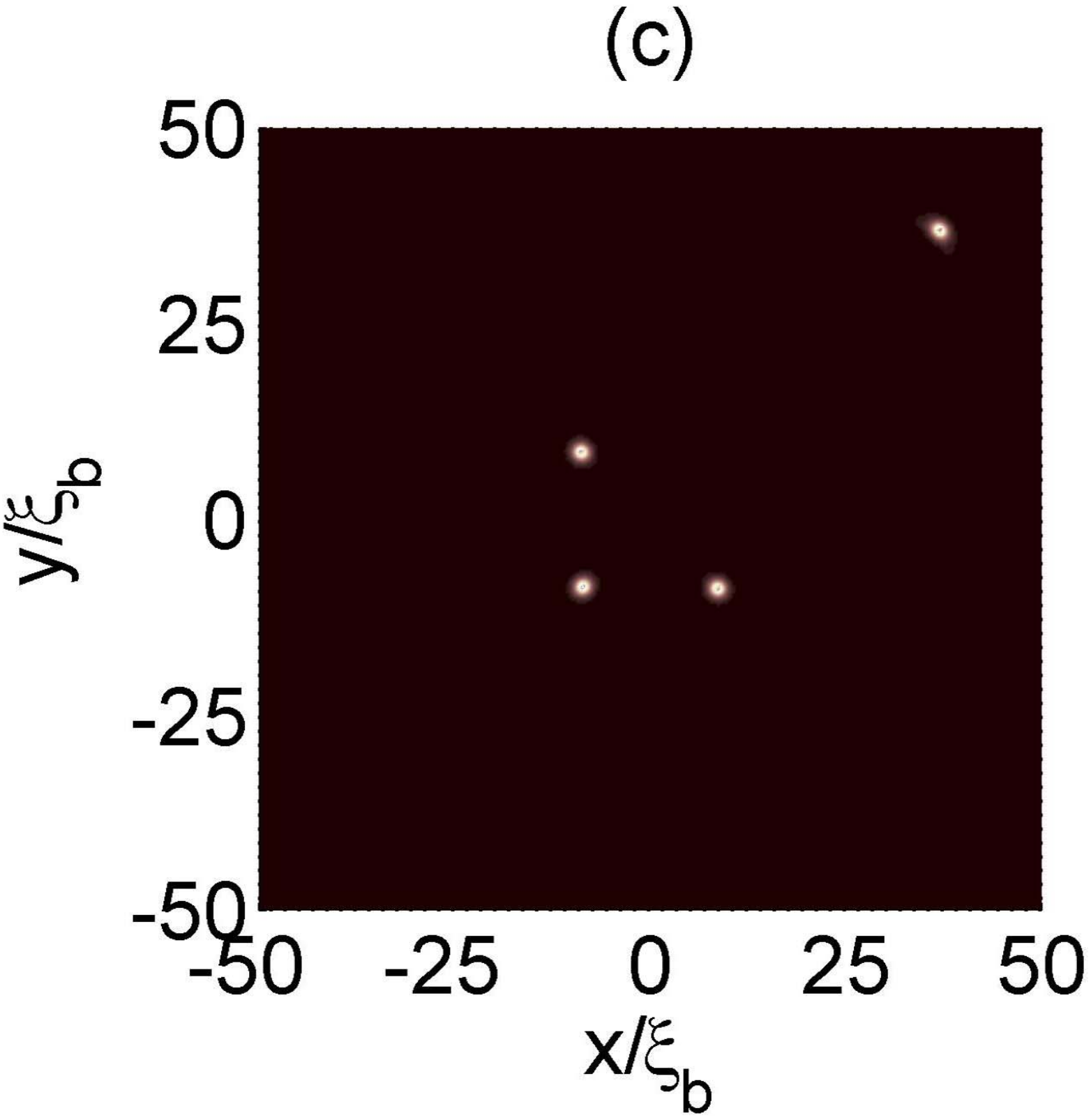
(c)
50
25
0
-25
-50
-50
-25
0
25
50
y/ξb
x/ξb

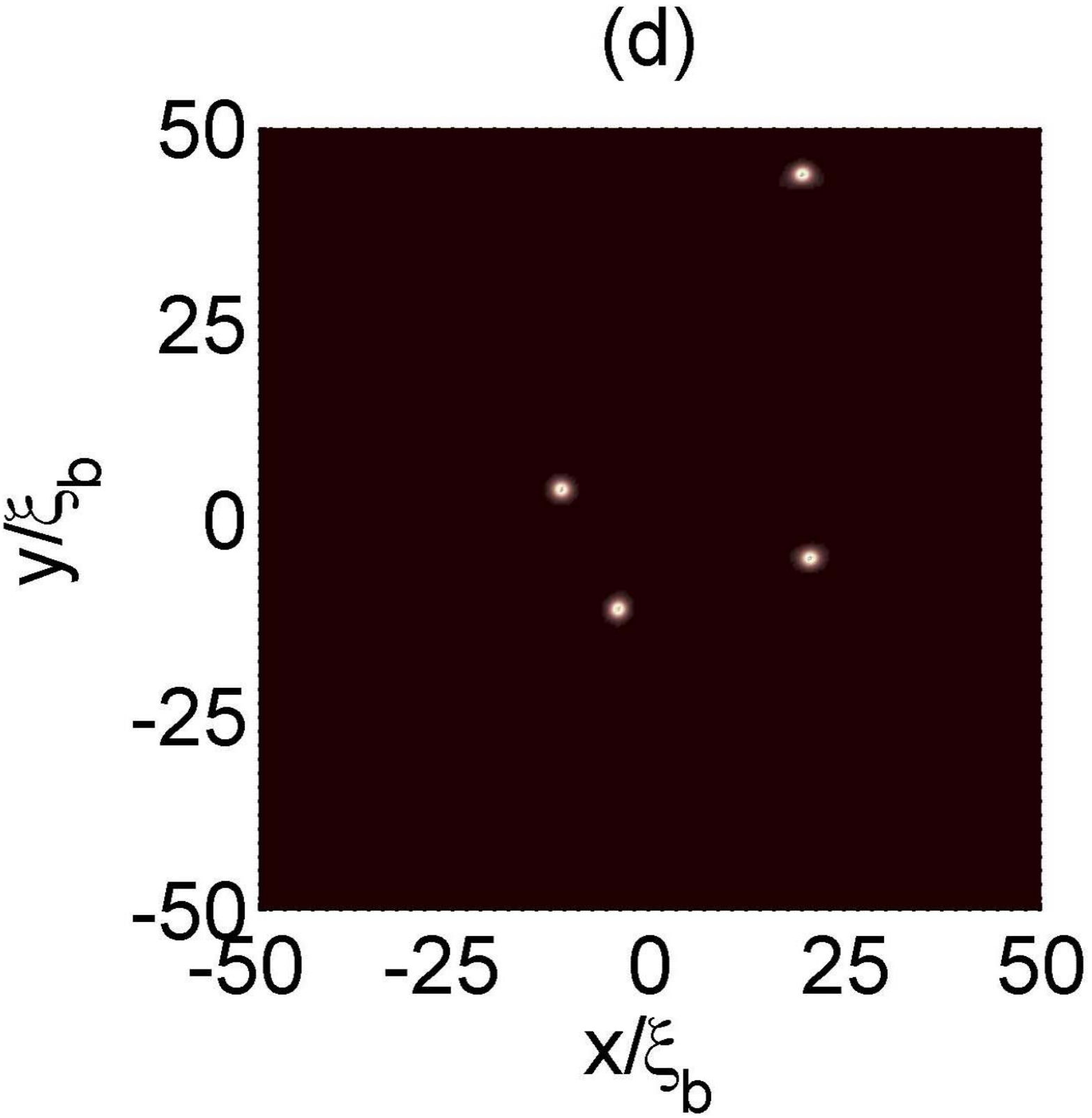
(d)
50
25
0
-25
-50
y/ξb
-50
-25
0
25
50
x/ξb